

Convective shutdown in a porous medium at high Rayleigh number

Duncan R. Hewitt^{1,†}, Jerome A. Neufeld^{1,2,3} and John R. Lister¹

¹Institute of Theoretical Geophysics, Department of Applied Mathematics and Theoretical Physics, University of Cambridge, Wilberforce Road, Cambridge CB3 0WA, UK

²Department of Earth Sciences, University of Cambridge, Downing Street, Cambridge CB2 3EQ, UK

³BP Institute, University of Cambridge, Bullard Laboratories, Madingley Road, Cambridge CB3 0EZ, UK

(Received 28 June 2012; revised 1 November 2012; accepted 4 January 2013;
first published online 19 February 2013)

Convection in a closed domain driven by a dense buoyancy source along the upper boundary soon starts to wane owing to the increase of the average interior density. In this paper, theoretical and numerical models are developed of the subsequent long period of shutdown of convection in a two-dimensional porous medium at high Rayleigh number Ra . The aims of this paper are twofold. Firstly, the relationship between this slowly evolving ‘one-sided’ shutdown system and the statistically steady ‘two-sided’ Rayleigh–Bénard (RB) cell is investigated. Numerical measurements of the Nusselt number Nu from an RB cell (Hewitt *et al.*, *Phys. Rev. Lett.*, vol. 108, 2012, 224503) are very well described by the simple parametrization $Nu = 2.75 + 0.0069Ra$. This parametrization is used in theoretical box models of the one-sided shutdown system and found to give excellent agreement with high-resolution numerical simulations of this system. The dynamical structure of shutdown can also be accurately predicted by measurements from an RB cell. Results are presented for a general power-law equation of state. Secondly, these ideas are extended to model more complex physical systems, which comprise two fluid layers with an equation of state such that the solution that forms at the (moving) interface is more dense than either layer. The two fluids are either immiscible or miscible. Theoretical box models compare well with numerical simulations in the case of a flat interface between the fluids. Experimental results from a Hele–Shaw cell and numerical simulations both show that interfacial deformation can dramatically enhance the convective flux. The applicability of these results to the convective dissolution of geologically sequestered CO_2 in a saline aquifer is discussed.

Key words: convection, convection in porous media, porous media

1. Introduction

Convective transport in porous media plays a significant role in a wide range of geophysical and industrial processes. The canonical system for the study of convection, and its associated nonlinear dynamics, is the Rayleigh–Bénard (RB) cell. The RB cell is a ‘two-sided’ convective system, in which there is convective transport away from both the upper and lower boundaries. The system therefore attains a statistically steady

† Email address for correspondence: drh39@cam.ac.uk

state, which allows both for examination of the dynamical structures and emergent patterns of the flow, and for accurate characterization of the convective flux.

Natural convective systems in porous media tend instead to be driven by a source of buoyancy on one boundary alone. We refer to such systems as ‘one-sided’. There are fundamental questions relating to the differences and similarities of the dynamics between one-sided and two-sided convective systems, some of which we address in this paper. For clarity, when we consider one-sided systems, we will assume throughout that the convective flow is downwards, away from an active upper boundary. All the other boundaries of the domain are assumed to be impermeable and perfectly insulating. Furthermore, we consider one-sided systems in which convection is driven solely by compositional density differences, such that the density ρ^* of the fluid is a function of the concentration of solute C^* only. It should be noted, however, that the governing equations outlined in § 3 are equally applicable to convection from a buoyant source at the base of the domain, and to thermal convection, provided that heat transfer in the solid phase of the medium can be neglected.

There has been a recent resurgent interest in the subject of one-sided convection in a porous medium owing to its relevance to the long-term storage of geologically sequestered carbon dioxide. With growing global demand for energy, it seems probable that sequestration will need to play a major role as a part of attempts to curb the rising anthropogenic emissions of CO_2 (Metz *et al.* 2005). Geological sequestration is achieved by injecting supercritical CO_2 into deep, brine-saturated porous rock, which is typically located at depths $\gtrsim 800$ m below the Earth’s surface and bounded above by an impermeable caprock. Under these storage conditions, the supercritical CO_2 is significantly less dense ($\sim 700 \text{ kg m}^{-3}$) than the ambient brine ($\sim 1000 \text{ kg m}^{-3}$), and will rise through the aquifer to pool beneath the caprock. Fractures in the caprock can lead to undesired leakage of the buoyant CO_2 plume (Pritchard 2007; Neufeld *et al.* 2011; Vella *et al.* 2011). One of the primary mechanisms for longer-term storage is the dissolution of CO_2 into the underlying ambient brine (Orr 2009), which forms a dense solute that can lead to downward convection. Geochemical field observations in natural CO_2 reservoirs suggest that convective dissolution provides a very significant and persistent mechanism for the transport of CO_2 (Gilfillan *et al.* 2009).

This paper has two principal objectives, which are related to the ideas of the previous paragraphs. Firstly, we examine the relationship between two-sided and one-sided convection with a fixed upper boundary. Secondly, we extend these ideas to examine different physically motivated one-sided systems, each of which comprises two fluid layers with a moving interface, such as in the case of sequestered CO_2 and brine.

Previous work on the two-dimensional porous RB cell has focused on examining the dimensionless heat (or solute) flux through the cell, as described by the Nusselt (or Sherwood) number Nu , and the corresponding dynamical structures of the flow. Both the Nusselt number and the dynamics of the flow are functions of the Rayleigh number Ra , which is the ratio of the diffusive and convective time scales. For $Ra < Ra_{crit} = 4\pi^2$, the system is stable, and there is no flow (Nield & Bejan 2006). For $4\pi^2 < Ra \lesssim 1300$, the flow is characterized by large-scale convective rolls, which undergo a series of bifurcations that perturb, but do not completely break down, the background flow (Kimura, Schubert & Strauss 1986; Graham & Steen 1994). However, above $Ra \approx 1300$, the rolls are broken down by vigorous plume shedding from the boundary layers at the top and bottom of the domain. The dynamical structure in this ‘high- Ra ’ regime is dominated by vertical columnar ‘megaplumes’ that extend across the interior of the domain, and are driven by entrainment and mixing of

small ‘protoplumes’ near the upper and lower boundaries (Otero *et al.* 2004; Hewitt, Neufeld & Lister 2012). Numerical measurements of the Nusselt number by Hewitt *et al.* (2012) could be approximately fitted over the range $1300 \lesssim Ra \leq 4 \times 10^4$ by a power-law scaling $Nu \sim Ra^{0.95}$. However, detailed examination of the results strongly suggests that asymptotically Nu scales linearly with Ra , and thus that the dimensional convective flux is asymptotically independent of the depth of the domain, in agreement with the ‘classical’ scaling argument for fluid convection (Howard 1964). In this paper we show that a function of the form $Nu = \alpha Ra + \beta$, for constant α and β , provides a significantly more accurate fit to the measurements of Hewitt *et al.* (2012) than a sub-linear power law, as discussed in § 4.2.2.

In contrast to the two-sided statistically steady RB configuration, the dynamics and the buoyancy flux in a one-sided convective system evolve over time. Many previous studies of one-sided convective systems have focused on the conditions required for the onset of convection, which presents significant theoretical challenges because the diffusive base state is both time-dependent and nonlinear. Various theoretical studies (Hassanzadeh, Pooladi-Darvish & Keith 2006; Riaz *et al.* 2006; Xu, Chen & Zhang 2006; Slim & Ramakrishnan 2010) have been complemented by direct numerical investigations (Riaz *et al.* 2006; Hassanzadeh, Pooladi-Darvish & Keith 2007) and laboratory experiments (Fernandez *et al.* 2002; Backhaus, Turitsyn & Ecke 2011; Slim *et al.* 2013) that explore the onset of convection.

After onset, the convective flow is dominated by large dense plumes, which merge and coarsen as they descend. These descending plumes are fed by the entrainment of smaller plumes near the upper boundary, which are themselves generated episodically by short-wavelength instabilities in the boundary layer. The system evolves independently of the depth of the domain until the largest plumes reach the lower boundary. There have been a number of numerical studies for $Ra \lesssim O(10^3)$ that examine the evolution of the dynamics and the merging of descending plumes before they interact with the lower boundary (Hassanzadeh *et al.* 2007; Pau *et al.* 2010). Slim *et al.* (2013) performed experiments in a Hele-Shaw cell for $100 < Ra < 1700$, and categorized the evolution of the system from the onset of convection in detail. Further experimental studies by Neufeld *et al.* (2010) for $5 \times 10^4 < Ra < 6 \times 10^5$ in a quasi-two-dimensional porous medium, and by Backhaus *et al.* (2011) for $6 \times 10^3 < Ra < 9 \times 10^4$ in a Hele-Shaw cell, provided measurements of the convective flux after the onset of convection.

When the descending plumes reach the lower boundary, the domain begins to fill up with dense fluid. Once this dense fluid reaches the upper boundary, the dynamics of the system change and the convective flux begins to decrease. The qualitative behaviour of the flux in this ‘shutdown’ regime has been observed in numerical simulations by Hassanzadeh *et al.* (2007) for $Ra < 1000$, although they provided no theoretical analysis of the system. Slim *et al.* (2013) presented experimental results in this regime for $100 < Ra < 1700$, and derived a phenomenological model that describes the evolution of the flux based on an *ad hoc* parametrization of the typical boundary-layer depth. We are not aware of any studies that explore the shutdown regime, in which the convective flux steadily decreases, for $Ra > 1700$.

In this paper we focus on examining the evolution of the dynamics and the convective flux during the shutdown regime for $Ra > O(10^3)$. In the first half of the paper, we show that the evolution of the flux in this one-sided problem can be directly calculated using measurements of the convective flux from an RB cell. We develop a simple theoretical ‘box’ model for this system that uses these measurements to predict the time scales for shutdown, and compare the results to high-

resolution numerical simulations. Furthermore, we find that the dynamical structure of the flow in the shutdown regime exhibits a remarkable similarity to that in an RB cell: the flow is dominated by vertical columnar ‘megaplumes’ that extend across the height of the domain, and the lateral spacing of these plumes increases as the average concentration increases and the system shuts down, in excellent quantitative agreement with measurements from an RB cell. Motivated by previous experimental systems (Neufeld *et al.* 2010; Backhaus *et al.* 2011) with a nonlinear density curve, we also examine how the rate of shutdown depends on the form of the density $\rho^*(C^*)$ by considering a power-law equation of state.

In the second half of the paper, we develop these ideas to model convective systems comprising two fluid layers, with an interface that is free to move. We examine the dynamics and evolution of these systems using a combination of simple theoretical box models, high-resolution numerical simulations and experiments. These tools allow us to investigate and understand the similarities and differences between a variety of physical systems, which are described in more detail in the following section. Finally, we use our models to estimate the time scales for convective shutdown in a reservoir with parameter values typical of those found in current CO₂ sequestration sites.

2. Overview of physical systems

We explore three different model systems for one-sided convection in a porous medium, each with different physical applications (figure 1). The systems are distinguished primarily by different properties of the active interface at the top of the convecting region: the first system is a ‘fixed-interface’ system, in the sense that the interface is stationary and is located at a fixed upper boundary; the second and third systems are ‘free-interface’ systems, in the sense that the active interface is free to move and divides the convecting region below from a non-convecting region of fluid above. The second and third systems are distinguished by whether the fluids on either side of the interface are immiscible or miscible, as discussed below.

In the first part of the paper, we consider the ‘fixed-interface’ system, in which the convective flux away from an interface does not significantly change its height. There are a broad range of geophysical systems for which this is an excellent approximation, including the convection of saline groundwater driven by evaporation at the upper surface (Duffy & Al-Hassan 1988; Wooding, Tyler & White 1997a; Wooding *et al.* 1997b), and the extraction of geothermal energy driven by underground heat sources (Cheng 1978; Goldstein *et al.* 2011). We consider a fluid that initially contains a dissolved solute at some concentration C_-^* . The upper boundary of the domain is held at a fixed larger concentration C_m^* . We consider a density curve that increases monotonically from $\rho^*(C_-^*)$ to $\rho_m^* = \rho^*(C_m^*)$. A typical density curve for such a system is shown schematically in figure 1(a), together with vertical profiles of the concentration and density. Diffusion of solute across the upper boundary forms a dense solution that is unstable to downwards convection. Over time, the concentration increases from C_-^* towards C_m^* , and convection gradually shuts down.

In the second part of the paper, we consider two different sorts of ‘free-interface’ system, in which the convective flux away from an interface causes the interface to move. These are typically two-component systems, which initially comprise a light fluid A overlying a dense fluid B. Dissolution of A into B creates fluid that is more dense than pure B. The system is thus unstable to convection, and the active interface between the two layers moves as A dissolves into B and convection transports the dense solution down into the lower layer. The concentration C^* describes that of

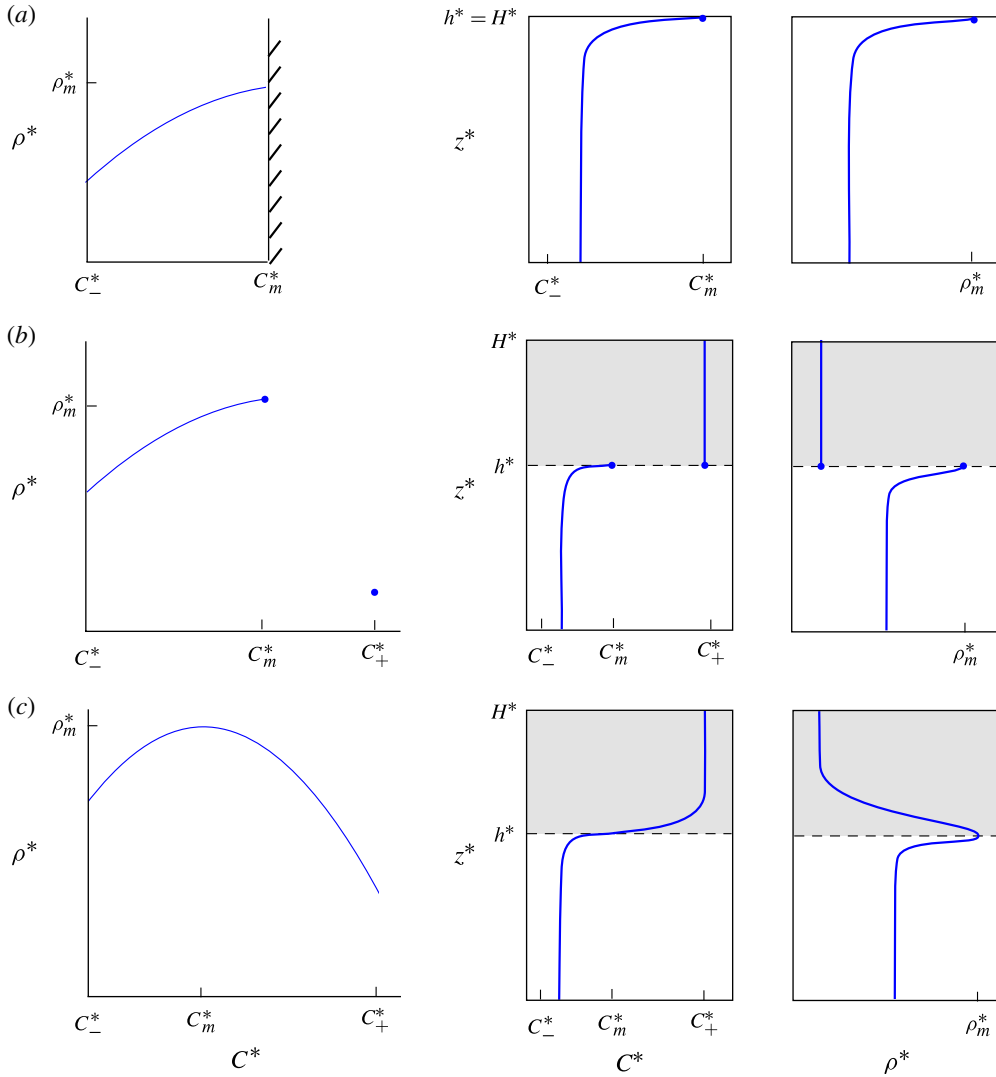


FIGURE 1. (Colour online) A schematic diagram showing typical equations of state $\rho^*(C^*)$, vertical concentration profiles $C^*(z^*)$ and vertical density profiles $\rho^*(z^*)$ for each of the three physical systems outlined in § 2: (a) the ‘fixed-interface’ system, with a stationary upper boundary $z^* = h^* = H^*$ held at concentration C_m^* ; (b) the ‘immiscible’ system, in which fluid with concentration C_+^* overlies fluid with initial concentration C_-^* , and the upper fluid is partially soluble in the lower; and (c) the ‘miscible’ system, in which the two fluids are fully soluble, and the interfacial height $z^* = h^*$ is given by the isopycnal of maximum density. In each case the maximum density ρ_m^* is attained at concentration C_m^* , the interfacial height is given by $z^* = h^*$ and the domain has constant depth H^* .

the solution of A in B, with pure A having concentration C_+^* , and pure B having concentration $C_-^* < C_+^*$. Mathematically, this is related to the classical Stefan problem (see e.g. Hill 1987), and our approach to the modelling is similar to that used for convection in a (non-porous) fluid layer below a melting interface (e.g. Huppert & Sparks 1988a,b; Huppert 1989).

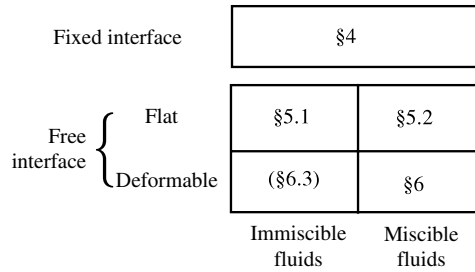


FIGURE 2. A diagram showing the layout of this paper, as discussed in detail in § 2. The case of immiscible fluids with a deformable interface is not studied in this paper, but is discussed in § 6.3.

We consider two qualitatively different free-interface systems, which correspond to immiscible and miscible fluids, respectively. In the ‘immiscible’ system, A is only partially soluble in B, and, for simplicity, we assume that B is not at all soluble in A. The density is largest ($\rho^* = \rho_m^*$) at the maximum concentration of A in B, denoted by C_m^* . The concentration C^* cannot lie in the range $C_m^* < C^* < C_+^*$, and, as such, there is a discontinuity in the concentration and density fields at the interface, which divides pure A above from a solution of A in B below. This behaviour can be seen in figure 1(b), which shows a typical density curve for the immiscible system, together with vertical profiles of the concentration and density.

In contrast, in the ‘miscible’ system A and B are fully soluble, and the equation of state $\rho^*(C^*)$ is continuous, with a maximum at some intermediate concentration C_m^* as shown schematically in figure 1(c). There is a qualitative distinction here from the immiscible system, in that there is not a genuine interface between different fluids when the fluids are miscible. Instead, we define the interface to be equal to the contour of maximum density ($\rho^* = \rho_m^*$). This isopycnal separates stably stratified fluid above from unstably stratified fluid below, and is therefore an interface in the sense that it lies between regions of dynamically different fluid behaviour.

Both immiscible and miscible systems have important applications, most pertinently to the subject of CO₂ sequestration. Supercritical CO₂ and brine are immiscible, with CO₂ being only 3–5% soluble by weight in brine under typical storage conditions (van der Meer 2005). In contrast, many experimental analogues of sequestration systems are based on mixtures of glycol and water, and form miscible systems (e.g. Neufeld *et al.* 2010; Backhaus *et al.* 2011).

The structure of the paper is as follows (see figure 2). In § 3 we present the governing equations, non-dimensionalization and numerical scheme used throughout the paper. In the subsequent sections, we develop a series of mathematical models that describe the different physical systems that we have introduced above.

Firstly, in § 4 we examine the ‘fixed-interface’ system. We develop a simple theoretical box model of this system, which describes the shutdown of the solute flux over time, and compare the results with high-resolution numerical simulations. The box model uses measurements of the flux from an RB cell. We also show that the dynamical structure of the flow in the one-sided system can be accurately predicted by measurements from an RB cell.

In § 5 we examine both immiscible and miscible free-interface systems under the assumption that the interface remains flat; the interface moves as fluid A dissolves into fluid B, but it remains planar and there is no entrainment across it. This assumption

allows us to use the results of the first part of the paper to derive theoretical box models of each system, which are compared with direct numerical measurements. For the immiscible system (§ 5.1), we make the additional modelling assumption that the pore space is always fully saturated: there is no capillary retention of fluid in the pores of the medium, and as such the interface remains ‘sharp’.

In § 6 we relax the assumption of a flat interface, and present experimental and numerical results for the miscible system when the interface is free to deform. The experimental system consists of water overlying propylene glycol in a Hele-Shaw cell. Solutions of these fluids have a density curve that is qualitatively similar to that shown in figure 1(c). We find that the effects of interfacial deformation and entrainment can be considerable in the miscible system. In contrast, in § 6.3 we argue that interfacial deformation is likely to be negligible in the immiscible system.

Finally, in § 7, we summarize the main results of this paper, and discuss the implications for the different physical systems.

3. Governing equations

3.1. Dimensional equations

We consider the flow of a Boussinesq fluid in a two-dimensional homogeneous isotropic porous medium, with horizontal and vertical coordinates x^* and z^* , respectively (dimensional variables are denoted with a $*$). We assume that the flow $\mathbf{u}^* = (u^*, w^*)$ obeys Darcy’s law and is incompressible,

$$\mathbf{u}^* = -\frac{\Pi}{\mu}(\nabla p^* + \rho^* g \hat{\mathbf{z}}^*), \tag{3.1}$$

$$\nabla \cdot \mathbf{u}^* = 0, \tag{3.2}$$

where Π is the permeability of the porous medium and μ is the fluid viscosity, both of which are assumed to be constant, p^* is the pressure field, g is the acceleration due to gravity, and $\hat{\mathbf{z}}^*$ is a unit vector in the positive z^* direction. The density ρ^* is a function of the local concentration C^* . The concentration C^* evolves in time t^* by advection and diffusion,

$$\phi \frac{\partial C^*}{\partial t^*} = -\mathbf{u}^* \cdot \nabla C^* + \phi D \nabla^2 C^*, \tag{3.3}$$

where ϕ is the porosity of the porous medium and D is the diffusivity, both again assumed to be constant, and for simplicity we have neglected the effects of dispersion. These equations are equally applicable to thermal convection, provided heat transfer in the solid phase of the medium can be neglected.

We consider the boundary and initial conditions for each of the different systems described in § 2. The fixed-interface system has a stationary active upper boundary. The domain has height h_0^* and width L^* . The upper boundary has an imposed constant concentration $C^*|_{z^*=h_0^*} = C_m^*$, and no vertical velocity, $w^*|_{z^*=h_0^*} = 0$. The lower and side boundaries have zero mass and buoyancy fluxes,

$$w^* = \frac{\partial C^*}{\partial z^*} = 0 \quad \text{at } z^* = 0, \quad u^* = \frac{\partial C^*}{\partial x^*} = 0 \quad \text{at } x^* = 0, L^*. \tag{3.4a,b}$$

The medium is initially saturated with fluid at a concentration $C_-^* < C_m^*$. The initial and boundary conditions for this system are shown schematically in figure 3(a), and the equation of state is discussed below.

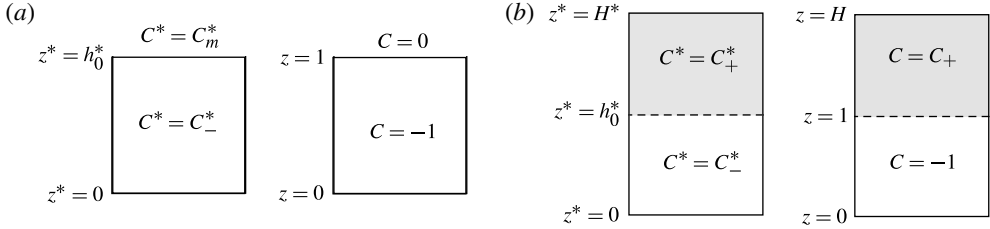


FIGURE 3. A schematic showing the initial conditions in both dimensional and dimensionless variables: (a) the fixed-interface system with a stationary upper active boundary; and (b) free-interface systems (either immiscible or miscible) with an interfacial height that evolves in time.

Free-interface systems (both immiscible and miscible) have an active interface that is located in the interior of the domain, and is free to move. The domain has a constant depth H^* and width L^* , with zero mass and buoyancy fluxes on every boundary,

$$w^* = \frac{\partial C^*}{\partial z^*} = 0 \quad \text{at } z^* = 0, H^*, \quad u^* = \frac{\partial C^*}{\partial x^*} = 0 \quad \text{at } x^* = 0, L^*. \quad (3.5a,b)$$

The medium is initially saturated with fluid in two layers (figure 3b): a lower layer of concentration C_-^* , and an upper layer of concentration $C_+^* > C_-^*$. The density of the lower layer $\rho_-^* = \rho^*(C_-^*)$ is greater than the density of the upper layer $\rho_+^* = \rho^*(C_+^*)$, and, as such, the system is stable to large-scale overturning. The initial height of the interface between the layers is given by $z^* = h_0^*$. For $t^* > 0$, the interfacial height is given by $z^* = h^*(x^*, t^*)$, which is defined to be the contour of maximum density $\rho^* = \rho_m^*$. The details of how the location of the interface is determined over time in each of the different model frameworks that we employ are discussed in §§ 5 and 6.

For both fixed-interface and free-interface systems, we consider general power-law equations of state,

$$\rho^* = \rho_m^*[1 - b(C_m^* - C^*)^n], \quad (3.6)$$

where $b > 0$ is a constant coefficient and n is a positive integer. The maximum density, given by the constant ρ_m^* , is attained at concentration C_m^* . For the fixed-interface system, the concentration C^* is always less than C_m^* , and so $\rho^*(C^*) \leq \rho_m^*$ irrespective of n . For immiscible free-interface systems, the concentration above the interface is fixed at $C^* = C_+^*$, while below the interface the concentration is again always less than C_m^* . For miscible free-interface systems, however, (3.6) holds for $C^* > C_m^*$, and so we require n to be an even (positive) integer in order to satisfy $\rho_+^* < \rho_-^*$. Representative equations of state for each system are shown in figure 1. In this paper we focus primarily on either linear ($n = 1$) or quadratic ($n = 2$) equations of state.

3.2. Dimensionless equations

For all the systems considered, we define a density scale $\Delta\rho^* = \rho_m^*b(C_m^* - C_-^*)^n$ to be the difference between the maximum density and the initial density of the lower layer, and a convective velocity scale $U^* = \Pi g \Delta\rho_m^*/\mu$. We also define the dimensionless interfacial height h , concentration C and density ρ to be

$$h = \frac{h^*}{h_0^*}, \quad C = \frac{C^* - C_m^*}{C_m^* - C_-^*}, \quad \rho = 1 + \frac{\rho^* - \rho_m^*}{\Delta\rho^*}. \quad (3.7a,b,c)$$

The dimensionless concentration below the interface is then negative, and $C = 0$ at the interface where the density is maximum ($\rho = 1$). We scale lengths with the initial interfacial height h_0^* , velocities with U^* , pressures with $\mu U^* h_0^* / \Pi$, and times with the convective time scale $T^* = \phi h_0^* / U^*$.

Rescaling in this way gives dimensionless governing equations

$$\mathbf{u} = -[\nabla P - (-C)^n \hat{\mathbf{z}}], \quad (3.8)$$

$$\nabla \cdot \mathbf{u} = 0, \quad (3.9)$$

$$\rho = 1 - (-C)^n, \quad (3.10)$$

$$\frac{\partial C}{\partial t} = -\mathbf{u} \cdot \nabla C + \frac{1}{Ra_0} \nabla^2 C, \quad (3.11)$$

with a reduced pressure $P = p + z / [\beta (C_m^* - C_-^*)^n]$, and an initial Rayleigh number

$$Ra_0 = \frac{h_0^* U^*}{\phi D} = \frac{h_0^* \Pi g \Delta \rho^*}{\phi D \mu}. \quad (3.12)$$

For the fixed-interface system, the dimensionless initial condition is $C(x, z, t = 0) = -1$, and the upper boundary condition is $C|_{z=1} = 0$. For free-interface systems, the dimensionless initial concentration profile is given by

$$C(x, z, t = 0) = \begin{cases} -1 & \text{for } 0 \leq z \leq 1, \\ C_+ & \text{for } 1 < z < H, \end{cases} \quad (3.13)$$

as shown schematically in figure 3.

3.3. Numerical method

The requirement of incompressibility (3.9) can be satisfied by introducing a streamfunction ψ , with $(u, w) = (\psi_z, -\psi_x)$. We can also eliminate the pressure field P by taking the curl of (3.8), which gives

$$\nabla^2 \psi = -\frac{\partial}{\partial x} (-C)^n. \quad (3.14)$$

Equations (3.11) and (3.14) were solved numerically, using the method that is briefly outlined here and discussed in more detail in appendix A. We anticipated a thin diffusive boundary layer below the interface $z = h(x, t)$ and, in order to ensure that the dynamics near the interface are well resolved, we used a vertical coordinate transformation $\zeta = f(z, h)$. For the free-interface systems, this transformation is adaptive, and is recalculated once the interface has moved a sufficient distance to require it. The horizontal and temporal resolution are uniform.

We solved the Poisson equation (3.14) using a spectral method in the horizontal direction, and a compact fourth-order finite-difference operator for the vertical derivatives. The diffusion and advection operators in the transport equation (3.11) were discretized using standard second-order finite differences and flux-conservative techniques, respectively, and the equation was solved using an alternating-direction implicit method (Press *et al.* 1989). The boundary conditions were imposed in such a way as to ensure that the numerical scheme retained second-order accuracy (see appendix A for details).

4. Fixed-interface system

We begin by considering a fixed-interface system, in which the active interface is located at the stationary upper boundary $z = 1$. In §4.1, we present the results of high-resolution numerical calculations. Motivated by these results, in §4.2 we derive a simple one-dimensional ‘box’ model of this system in the shutdown regime. We develop the box model using measurements of $Nu(Ra)$ from an RB cell. In §4.3, we compare this theoretical box model with the numerical results. Finally, in §4.4, we compare the dynamical structure of the flow with that of an RB cell.

In §3.2, we non-dimensionalized the variables with respect to the advective time scale T^* . The dimensionless diffusive solute flux through the upper boundary is therefore given by $Ra_0^{-1} \partial C / \partial z|_{z=1}$ (from (3.11)). However, we are aiming to compare the one-sided system with the RB cell, where the dimensionless flux is more commonly defined with respect to the diffusive time scale (as in, for example, standard definitions of the Nusselt number). It is thus helpful to consider a rescaled flux, which we define to be the actual dimensionless flux scaled by the flux Ra_0^{-1} that would be given by diffusion down a unit linear concentration gradient in the absence of convection. The horizontally averaged rescaled flux $F(t)$ is therefore given by

$$F(t) = \frac{1}{L} \int_0^L \left. \frac{\partial C}{\partial z} \right|_{z=1} dx. \quad (4.1)$$

Throughout this paper, we measure and model the rescaled flux $F(t)$.

4.1. Numerical results

Numerical snapshots of the concentration field $C(x, z, t)$ are shown in figure 4, together with the horizontally averaged concentration profile $\bar{C}(z, t) = L^{-1} \int_0^L C dx$ at different times, for a linear equation of state ($n = 1$) and an initial Rayleigh number $Ra_0 = 10^4$. The corresponding average solute flux $F(t)$ (figure 5) will be discussed in detail at the end of this subsection.

Initially, a stable diffusive boundary layer grows below the upper boundary. After a critical time $t_c \sim Ra_0^{-1}$ (see e.g. Riaz *et al.* 2006), the boundary layer becomes unstable to short-wavelength instabilities, leading to downward convection (figure 4a). At this point, both the flux from the upper boundary and the convective dynamics are independent of the location of the lower boundary. At some time t_1 , the first generation of convecting plumes reaches the base of the domain (figure 4b), while at some later time t_2 , the return flow from this interaction reaches the upper boundary and the flux begins to decrease. For $t > t_2$ the system enters a different, ‘shutdown’, regime in which the solute flux $F(t)$ decreases as the interior of the domain becomes steadily more concentrated with solute. The times t_1 and t_2 are controlled both by the diffusive onset time scale $t_c \sim Ra_0^{-1}$ and by the $O(1)$ convective time scale. Since $Ra_0 \gg O(1)$, we expect the convective time to dominate: thus t_1 can be assumed to be independent of Ra_0 , and $t_2 \approx 2t_1$. We find numerically that $t_1 \approx 7.5$ and $t_2 \approx 15$, in broad agreement with the experimental results of Slim *et al.* (2013). For $t > t_2$, the horizontally averaged concentration $\bar{C}(z, t)$ is approximately independent of z away from the boundary layer, and \bar{C} increases steadily over time (figure 4c,d). These observations underpin the theoretical modelling in §4.2.

The dynamics in the shutdown regime, $t > t_2$, are dominated by persistent descending ‘megaplumes’ interleaved with a columnar return flow that rises towards the upper boundary. Instabilities in the thin boundary layer at the upper boundary drive the growth of small vigorous ‘protoplumes’, which carry dense fluid from

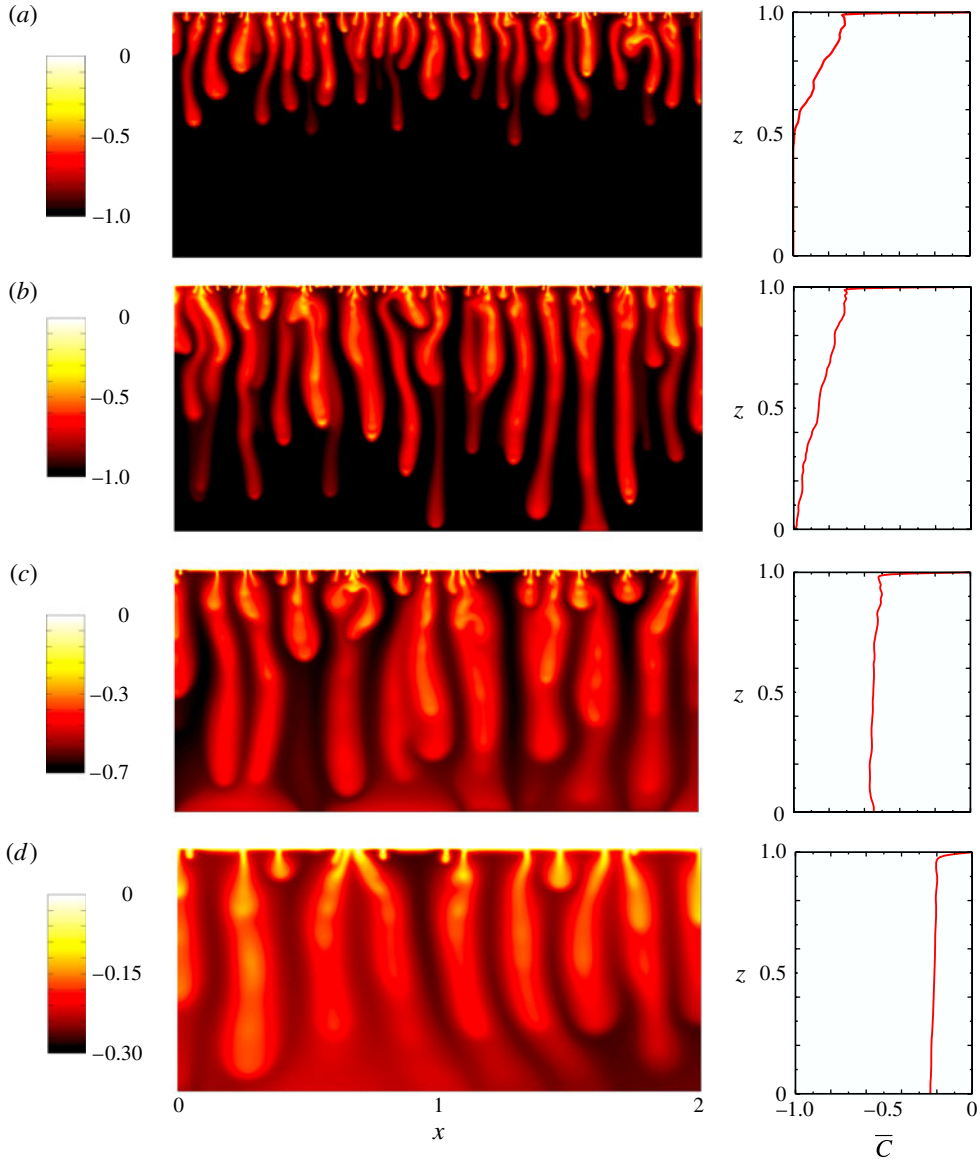


FIGURE 4. (Colour online) Snapshots of the concentration field C in a fixed-interface system, from numerical simulations, for $n = 1$, $Ra_0 = 10^4$ and aspect ratio $L = 2$, together with plots of the horizontally averaged concentration profile $\bar{C}(z, t) = L^{-1} \int_0^L C \, dx$: (a) time $t = 4$, before the first generation of plumes has reached the base of the domain; (b) $t = 8 \approx t_1$, when the descending plumes first reach the base; (c) $t = 32$, in the shutdown regime; and (d) $t = 128$. The horizontally averaged concentration profile in panels (c) and (d) is approximately uniform away from the upper boundary. The horizontal spacing of the downwelling plumes increases over time. Note the different grey (colour) scales on the left.

the boundary layer into the larger descending megaplumes. As the interior becomes more concentrated, the dynamics of the flow become less vigorous; the depth of the boundary layer increases as the density contrast with the interior decreases; and the

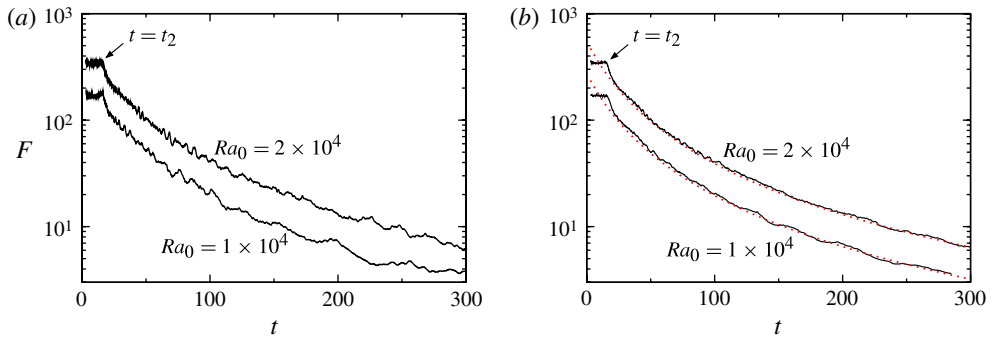


FIGURE 5. (Colour online) The horizontally averaged solute flux $F(t)$ (4.1), for a linear equation of state $n = 1$, aspect ratio $L = 2$ and $Ra_0 = 1 \times 10^4$ and 2×10^4 as marked: (a) measurements from one numerical simulation, showing the variability of F ; and (b) measurements ensemble-averaged over eight numerical simulations (solid), together with the theoretical predictions (4.15) (dotted) as discussed in § 4.2. The transition to the shutdown regime at $t = t_2$ is marked.

(differing) horizontal length scales associated with both protoplumes and megaplumes increase. The dynamical structure of the flow appears qualitatively very similar to that of the upper half of an RB cell in the high- Ra regime (Hewitt *et al.* 2012). This similarity is discussed in § 4.2.1.

The horizontally averaged solute flux (4.1) exhibits rapid chaotic fluctuations about a time-varying mean. Measurements of other variables from our numerical calculations also show some chaotic variation about time-varying average values. We typically ensemble-average our numerical results to reduce the fluctuations and to give clearer measurements for comparison with the theoretical modelling. The variables used in the theoretical sections of this paper refer to the mean values. The number of repeat simulations used in an ensemble average is given in the caption of the relevant figure.

Figure 5 shows numerical measurements of the horizontally averaged flux $F(t)$. The chaotic variation discussed above can be observed in measurements from a single simulation (figure 5a). Ensemble-averaged measurements (figure 5b) show that the flux initially fluctuates about an approximately constant value. Once the first generation of plumes have reached the lower boundary, and the domain has filled up with denser fluid, the flux decays slowly in the shutdown regime $t > t_2$.

4.2. Theoretical box model

The numerical calculations showed that the horizontally averaged interior concentration is approximately uniform for $t > t_2$ (figure 4c,d), apart from in a thin boundary layer near the upper boundary. This observation provides the motivation for the development of a simple box model, using a well-mixed approximation. We assume that, outside the thin boundary layer, the horizontally averaged concentration is independent of z , so that

$$\bar{C} = \Theta(t) \leq 0. \quad (4.2)$$

As $\Theta(t)$ increases towards zero, the strength of convection decreases. Based on the definition of the Rayleigh number in (3.12), we define a time-dependent Rayleigh number $Ra(t)$ to be proportional to the current density difference between the upper

boundary ($C = 0$) and the interior ($C = \Theta(t) \leq 0$). Thus

$$Ra(t) = Ra_0 |\Theta(t)|^n. \tag{4.3}$$

We further define a time-dependent Nusselt number $Nu(t)$, by scaling the flux $F(t)$ up to a unit concentration difference, which gives

$$Nu(t) = \frac{F(t)}{|\Theta(t)|}. \tag{4.4}$$

We expect $Nu(t)$ to be given by some function of the current Rayleigh number, so that $Nu(t) = \mathcal{N}[Ra(t)]$. The functional form of $\mathcal{N}(Ra)$ is discussed in § 4.2.2.

We integrate the transport equation (3.11) over the whole domain, and use the boundary conditions to obtain

$$\frac{d}{dt} \int_0^1 \int_0^L C \, dx \, dz = \frac{1}{Ra_0} \int_0^L \left. \frac{\partial C}{\partial z} \right|_{z=1} dx. \tag{4.5}$$

Using (4.1) and the definition of the horizontally averaged concentration $\bar{C}(z, t)$, (4.5) can be rewritten as

$$\frac{d}{dt} \int_0^1 \bar{C} \, dz = \frac{F}{Ra_0}. \tag{4.6}$$

Since, under the well-mixed approximation (4.2), we are neglecting the area of the thin boundary layer, (4.6) can be combined with (4.2) and (4.4) to give

$$\frac{d\Theta}{dt} = \frac{|\Theta|}{Ra_0} \mathcal{N}[Ra(t)]. \tag{4.7}$$

Equation (4.7) gives a theoretical prediction for the evolution of the shutdown regime, which we can solve for a given form of the Nusselt number $\mathcal{N}(Ra)$.

The model applies for $t > t_2$, and so (4.7) can be solved together with an initial condition for the interior concentration $\Theta(t_2)$. In fact, solutions can be extrapolated back to $t < t_2$, and (4.7) can thus be solved with an initial condition $\Theta(t_0) = -1$, where $t_0 < t_2$ is a virtual origin that allows for the differing dynamics of the system before it enters the shutdown regime. We find numerically that $t_0 = 0$ provides a very good approximation.

4.2.1. Relationship to the two-sided Rayleigh–Bénard cell

As noted earlier, the dynamical structure of one-sided flow in the shutdown regime (figure 4c,d) appears qualitatively very similar to half of the convective profile observed in a two-sided RB cell (Hewitt *et al.* 2012). We now show that the Nusselt number $\mathcal{N}_{RB}(Ra)$ measured in an RB cell is quantitatively applicable to shutdown in the one-sided system.

We consider first, for simplicity, the case of a linear equation of state ($n = 1$). Suppose that a statistically steady RB cell has boundary conditions of constant concentration $C = 0$ on the upper boundary and $C = -1$ on the lower, and an average concentration $C_{RB}^i = -1/2$ in the interior. As $n = 1$, the density difference $\Delta\rho_{RB}$ between the upper boundary and the interior is given by $\Delta\rho_{RB} = -C_{RB}^i = 1/2$. In contrast, while the one-sided system also has a boundary condition of $C = 0$ on the upper boundary, it has a condition of no solute flux through the lower boundary, and an average interior concentration $C^i = \Theta(t)$. The density difference between the upper boundary and the interior is therefore given by $\Delta\rho = |\Theta(t)|$.

We compare the two systems by rescaling $Ra(t)$ to take account of the different boundary conditions and density differences between the upper boundary and the interior. Firstly, because of the different lower boundary conditions, we suggest that the one-sided system is related to the upper half of an RB cell of double the depth. Secondly, in order that the density difference should agree in the two systems, we require the total density difference across the RB cell to be scaled by a factor $\Delta\rho/\Delta\rho_{RB} = 2|\Theta|$. The factor $\Delta\rho = |\Theta|$ is already included in the definition (4.3) of $Ra(t)$, and we therefore define the effective Rayleigh number Ra_e for the equivalent RB cell to be $Ra_e = 4Ra(t)$.

For the general case with a nonlinear equation of state ($n > 1$), we can perform a similar analysis. However, there are two differences. Firstly, the interior concentration C_{RB}^i of the RB cell is a function of n , as discussed in appendix B. Secondly, the dimensionless density difference is not simply equal to the concentration difference, but is given by $\Delta\rho_{RB} = |C_{RB}^i|^n$ and $\Delta\rho = |\Theta|^n$. Therefore, the effective Rayleigh number is given by

$$Ra_e = r(n)Ra(t), \quad \text{where } r(n) = \frac{2}{\Delta\rho_{RB}}, \quad (4.8a,b)$$

because, again, the factor $\Delta\rho = |\Theta|^n$ is already included in the definition (4.3) of $Ra(t)$. In appendix B we provide numerical estimates of $C_{RB}^i(n)$, and show that it can be well approximated by the empirical formula $C_{RB}^i = -(n+1)^{-1/n}$ for $n \leq 5$. Thus, $\Delta\rho_{RB}(n) = 1/(n+1)$, and the constant premultiplying factor $r(n)$ reduces to

$$r(n) = 2(n+1). \quad (4.9)$$

4.2.2. The functional form of the Nusselt number

In an RB cell, the time-averaged Nusselt number Nu is a function of the Rayleigh number Ra only, and is given by the form $\mathcal{N}_{RB}(Ra)$. Hewitt *et al.* (2012) showed that \mathcal{N}_{RB} asymptotically scales linearly with Ra . Typically, the relationship $\mathcal{N}_{RB}(Ra)$ is described as a slightly sub-linear power law for $Ra > 10^3$ (Otero *et al.* 2004; Neufeld *et al.* 2010; Backhaus *et al.* 2011). However, we find that the numerical measurements of $\mathcal{N}_{RB}(Ra)$ for $1300 < Ra < 4 \times 10^4$ from Hewitt *et al.* (2012) are more accurately fitted by an equation of the form

$$\mathcal{N}_{RB}(Ra) = \alpha Ra + \beta, \quad (4.10)$$

where $\alpha \approx 6.9 \times 10^{-3}$ and $\beta \approx 2.75$ are constants. Figure 6 shows a plot of \mathcal{N}_{RB}/Ra against Ra , together with (4.10) and the power-law curve $\mathcal{N}_{RB} \sim Ra^{0.95}$ that best fits the data. We find that the linear fit (4.10) deviates from the data by less than 0.6%, while the power-law fit deviates by more than 2%, over the range shown.

4.2.3. Analytic solution of the box model

The effective Rayleigh number $Ra_e = rRa_0 |\Theta|^n$, given by (4.3) and (4.8a), can be combined with (4.10) to give an expression for the Nusselt number in the one-sided system:

$$\mathcal{N}[Ra(t)] = \mathcal{N}_{RB}[Ra_e], \quad (4.11)$$

$$= \alpha rRa_0 |\Theta(t)|^n + \beta. \quad (4.12)$$

We use (4.12) to integrate (4.7) analytically. As discussed above, we take an initial condition $\Theta(t_0) = -1$, where $t_0 < t_2$ is a virtual time origin. The solution is

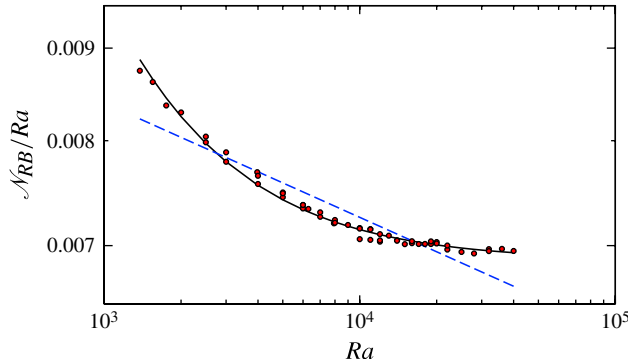


FIGURE 6. (Colour online) Measurements of the Nusselt number \mathcal{N}_{RB} divided by the Rayleigh number Ra in an RB cell from Hewitt *et al.* (2012). Equation (4.10) is also shown (solid), together with the best-fit power law $\mathcal{N}_{RB} \sim Ra^{0.95}$ (dashed).

given by

$$\Theta(t) = -\gamma^{1/n} [(1 + \gamma)e^{\alpha\gamma nr(t-t_0)} - 1]^{-1/n}, \quad (4.13)$$

where $\gamma = \beta/(\alpha r Ra_0)$.

If Ra_0 is sufficiently large ($Ra_0 \gg 10^3$) then $\gamma \ll 1$. In the limit $\gamma \rightarrow 0$, which corresponds to the simple asymptotic linear scaling $\mathcal{N} = \alpha r Ra$ in (4.12), equation (4.13) reduces to

$$\Theta(t) = -[1 + \alpha nr(t - t_0)]^{-1/n}, \quad (4.14)$$

and the solute flux $F(t)$, given by (4.4), becomes

$$F(t) = \alpha r Ra_0 |\Theta|^{n+1} = \alpha r Ra_0 [1 + \alpha nr(t - t_0)]^{-(n+1)/n}. \quad (4.15)$$

Thus, in the limit of large Ra_0 ($\gamma \rightarrow 0$), the evolution of the interior concentration $\Theta(t)$ becomes independent of Ra_0 , and the flux $F(t)$ is proportional to Ra_0 (as we might expect from the Nusselt number scaling), but otherwise evolves independently of Ra_0 .

An important feature of these results is the length of time it takes for the convective flux to shut down. The rate at which the flux F decreases is controlled by α , the constant in the Nusselt number relationship (4.10). Since $\alpha \ll 1$, the time scales for the shutdown of convection are much greater than the $O(1)$ convective time scale.

The dependence on the equation of state (3.10) of both the flux and the interior concentration is different at early and late times (figure 7). Initially, the flux decreases more rapidly at larger values of n . This behaviour can be seen from leading-order expansions of (4.14) and (4.15) (with $t_0 = 0$), which show that

$$\Theta = -[1 - \alpha r t + O(\alpha^2 t^2)], \quad F = \alpha r Ra_0 [1 - (n+1)\alpha r t + O(\alpha^2 t^2)]. \quad (4.16a,b)$$

Therefore, using (4.9), to leading order, one has $d\Theta/dt \sim 2\alpha(n+1)$ and $dF/dt \sim -4\alpha^2(n+1)^3$, both of which increase in magnitude with n . However, at late times, (4.14) and (4.15) are dominated by different scalings with time: the model predicts that the interior concentration $\Theta(t)$ increases towards zero like $t^{-1/n}$, and the flux $F(t)$ decays like $t^{-(n+1)/n}$. Therefore, the increase of the interior concentration and the resulting decrease of the flux are both ultimately slower at larger n .

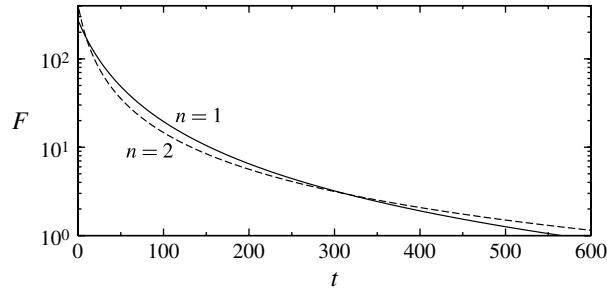


FIGURE 7. The solute flux $F(t)$ given by (4.15) for $Ra_0 = 10^4$, $n = 1$ (solid) and $n = 2$ (dashed), illustrating that the initial decrease of the flux is faster at larger n , while the long-time decay is slower and the flux is predicted to scale with $t^{-(n+1)/n}$.

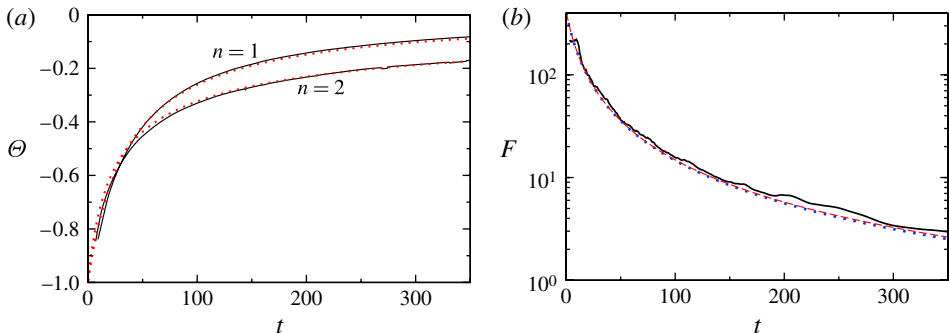


FIGURE 8. (Colour online) Measurements from full numerical calculations (solid) together with theoretical predictions, for $Ra_0 = 10^4$ and aspect ratio $L = 2$: (a) the interior concentration $\Theta(t)$, ensemble-averaged over four calculations, for $n = 1$ and $n = 2$ as marked, together with the theoretical predictions from (4.13) (dotted); (b) the solute flux $F(t)$ for $n = 2$, ensemble-averaged over four calculations, together with the theoretical prediction from (4.4) and (4.13) (dashed), and the theoretical prediction in the asymptotic limit $\gamma \rightarrow 0$ from (4.15) (dotted). Numerical measurements of $F(t)$ for $n = 1$ are shown in figure 5.

These differences can be understood by the shape of the density curve $\rho(C) = 1 - (-C)^n$ in (3.10) for different values of n . At larger n , the gradient of the density curve near $C = -1$ is larger, and therefore the density difference $|\Theta|^n$ that drives convection initially decreases more rapidly. However, the different scaling behaviour of $\rho(C)$ near to the stationary point $C = 0$ means that the long-time scaling of $F(t)$ and $\Theta(t)$ has a weaker exponent at larger n .

4.3. Comparison of the box model and numerical results

In this section we compare the analytic solutions with numerical measurements. We find empirically that $t_0 = 0$ gives good agreement with the numerical results, and therefore we use this value throughout.

The interior average concentration $\Theta(t)$ is measured in the numerical simulations by defining a time-dependent boundary-layer depth, below which the concentration is averaged in both spatial directions. Figure 8(a) shows numerical measurements and theoretical predictions of $\Theta(t)$, for both a linear ($n = 1$) and a quadratic ($n = 2$)

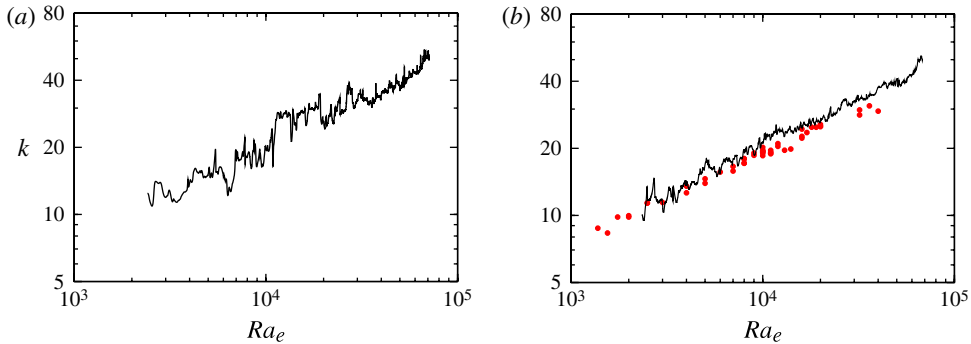


FIGURE 9. (Colour online) Numerical measurements of the average wavenumber k of the downwelling megaplumes, for a linear equation of state $n = 1$, an aspect ratio $L = 2$ and $Ra_0 = 2 \times 10^4$, measured at $z = 0.5$ and plotted against the effective Rayleigh number $Ra_e = 4Ra_0|\Theta|$ (4.8a,b): (a) measurements from one simulation, showing the typical variability of k ; and (b) measurements ensemble-averaged over eight simulations (solid line), together with direct measurements of $k(Ra_e)$ in an RB cell (points), taken from Hewitt *et al.* (2012).

equation of state. The theoretical predictions from the box model (4.13) give very good agreement with the full numerical solutions.

Figure 8(b) shows numerical measurements of the solute flux $F(t)$ for a quadratic equation of state ($n = 2$). The theoretical solution derived from (4.13) and the simpler asymptotic solution (4.15) are also shown. These solutions are almost indistinguishable from each other except at late times. Both solutions give excellent agreement with the numerical results.

These figures show that simple one-dimensional box models give a very good description of the evolution of the system in the shutdown regime. We have also shown that the results from an RB cell can be used both qualitatively and quantitatively to describe the average behaviour of the flux in the shutdown regime, and the corresponding evolution of the interior concentration Θ . Moreover, these results suggest that the simple asymptotic linear scaling $\mathcal{N} = \alpha r Ra$, with $\alpha = 6.9 \times 10^{-3}$ and $r(n)$ given by (4.9), is a very good approximation provided $Ra_0 > 10^3$.

4.4. Dynamical structure of shutdown: the horizontal wavenumber

The correspondence between one-sided and two-sided convection is further strengthened by a comparison of the dynamical structure of the flow. Figure 4 shows that, in the shutdown regime, the flow is dominated by long descending megaplumes, with an average horizontal wavenumber that decreases over time. Based on the discussion above, we might expect the average horizontal wavenumber $k(t)$, which will depend on the time-dependent Rayleigh number $Ra(t)$, to be in agreement with the equivalent dependence $k(Ra_e)$ from an RB cell.

We measured the average horizontal wavenumber $k(t)$ by taking the Fourier transform of the concentration profile at $z = 0.5$, and calculating the average value of k from the Fourier spectrum. Figure 9 shows this measured k as a function of $Ra_e = rRa(t)$, together with numerical results from Hewitt *et al.* (2012) for $k(Ra_e)$ in an RB cell. The good agreement seen in this figure provides further evidence that the one-sided system can be quantitatively compared to the upper half of an RB cell, and

that the dynamical structures of the shutdown regime are well described by the results from an RB cell.

5. Free-interface systems I: flat interface

In the first half of this paper we examined the shutdown of convection in a ‘fixed-interface’ system, and demonstrated the close link between such a one-sided system and the two-sided RB cell. In the second half of the paper, we develop these ideas to model different ‘free-interface’ systems, in which the flux of solute across an interface causes that interface to move. As described in § 2, such systems comprise two fluids that can be either immiscible or miscible: in an immiscible system, the upper fluid is only partially soluble in the lower, and (by assumption) the lower is not at all soluble in the upper; while in a miscible system, the upper fluid is fully soluble in the lower. For both immiscible and miscible systems, dissolution of the upper fluid into the lower causes a change in the density of the solution, which drives convection. Typical equations of state, average concentration profiles, and average density profiles for immiscible and miscible systems can be seen in figure 1(*b,c*).

In this section, we consider both immiscible and miscible systems under the assumption that the moving interface can be approximated as remaining flat. Therefore, the interfacial height h is a function of time alone. In § 5.1, we examine the immiscible system with a flat interface: we develop a simple one-dimensional box model, and compare the theoretical predictions of this model with measurements from full numerical simulations. In § 5.2, we examine the miscible system with a flat interface: we similarly present a theoretical one-dimensional box model and full numerical simulations. The reader is reminded that the ‘interface’ for the miscible system is defined by the isopycnal of maximum density (see § 2). In § 5.3, we summarize the main results of this section, and compare the two systems. In § 6, we relax the assumption of a flat interface and examine the effects of interfacial deformation for the miscible system.

The relevant variables and non-dimensionalization for free-interface systems were introduced in § 3. We recall that the system is initially stratified in two layers (figure 3*b*), with a lower layer $0 < z < 1$ of concentration -1 and an upper layer $1 < z < H$ of concentration $C_+ > 0$. The maximum density is attained at $C = 0$. The density is given as a function of the concentration by (3.10). For $t > 0$, the interfacial height is a function of time alone (due to the assumption of a flat interface), and is given by $z = h(t)$.

As in § 4, we consider the flux scaled by the diffusive flux in the absence of convection. Under the assumption of a flat interface, the scaled horizontally averaged flux $F(t)$ across the interface is given by

$$F(t) = \frac{1}{L} \int_0^L \left. \frac{\partial C}{\partial z} \right|_{z=h(t)} dx. \quad (5.1)$$

The evolution of the interfacial height $h(t)$ can be calculated from conservation of solute over the entire domain, which gives

$$\int_0^H \int_0^L C(x, z, t) dx dz = L[-1 + (H - 1)C_+]. \quad (5.2)$$

The right-hand side of (5.2) is the result of evaluating the integral at $t = 0$.

5.1. Immiscible system

When the two fluids are immiscible (and, by assumption, the lower fluid is insoluble in the upper), the concentration C_+ above the interface $z > h(t)$ remains constant, as does the corresponding density $\rho_+ < 0$. Hence global conservation of solute (5.2) reduces to

$$\int_0^{h(t)} \bar{C} \, dz = -1 + [h(t) - 1]C_+. \quad (5.3)$$

5.1.1. Theoretical box model

Following the analysis of § 4.2, we use a well-mixed approximation for the interior of the system in $z < h(t)$: we assume that, below a thin boundary layer, the horizontally averaged concentration $\bar{C}(z, t)$ is independent of z , and is given by

$$\bar{C} = \Theta(t) \leq 0. \quad (5.4)$$

Starting from the definition of the initial Rayleigh number (3.12), we now define the time-dependent Rayleigh number $Ra(t)$ to be

$$Ra(t) = Ra_0 |\Theta(t)|^n h(t), \quad (5.5)$$

which accounts for the changes in concentration and depth of the convecting layer. We further define a time-dependent Nusselt number $Nu(t)$, by scaling the horizontally averaged flux F up to a unit concentration difference and height, which gives

$$Nu(t) = \frac{h(t)F(t)}{|\Theta(t)|}. \quad (5.6)$$

The Nusselt number is given by the functional form $Nu(t) = \mathcal{N}[Ra(t)]$, as discussed in § 4.2.2, and the flux $F(t)$ is given by (5.1).

As in § 4.2, we integrate the transport equation (3.11) over the lower layer $z \leq h$, and use the boundary conditions together with (5.1) to obtain

$$\frac{d}{dt} \int_0^{h(t)} \bar{C} \, dz = \frac{F}{Ra_0}. \quad (5.7)$$

Under the well-mixed approximation (5.4), contributions to the area integral in (5.7) from the thin boundary layer below the interface are neglected. Equations (5.4), (5.6) and (5.7) can be combined to give

$$h \frac{d\Theta}{dt} = \frac{|\Theta|}{hRa_0} \mathcal{N}[Ra(t)]. \quad (5.8)$$

Equation (5.8) can be compared to (4.7), which is the equivalent governing equation for the fixed-interface box model.

The well-mixed approximation (5.4) can also be combined with global conservation of solute (5.3) to give

$$h\Theta = -1 + (h - 1)C_+, \quad (5.9)$$

which can be rearranged to obtain the interfacial height

$$h(t) = \frac{C_+ + 1}{C_+ + |\Theta(t)|}. \quad (5.10)$$

One could solve (5.8) and (5.10) numerically using any functional form of the Nusselt number $\mathcal{N}(Ra)$, including the numerical parametrization in (4.12). We have

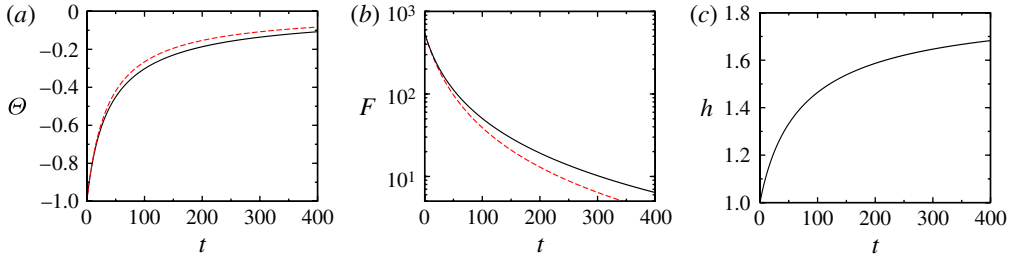


FIGURE 10. (Colour online) Theoretical results for the immiscible system with $n = 1$, $C_+ = 1.2$, $t_0 = 0$ and $Ra_0 = 2 \times 10^4$: (a) the average concentration $\Theta(t)$ given implicitly by (5.12) (solid), together with the prediction for a stationary interface given by (4.14) (dashed); (b) the solute flux $F(t)$ given by (5.13) (solid), together with the prediction for a stationary interface given by (4.15) (dashed); and (c) the interfacial height $h(t)$ given by (5.10) and (5.12).

shown in § 4 that the asymptotic linear scaling $\mathcal{N}(Ra) = \alpha r Ra$, where $\alpha = 6.9 \times 10^{-3}$ and $r(n)$ is defined in (4.9), provides a very good approximation to (4.12) if $Ra > 10^3$, and we therefore use this scaling here. Equations (5.8) and (5.10), together with this linear scaling, give a simple ordinary differential equation for Θ :

$$\left(\frac{C_+ + 1}{C_+ + |\Theta|} \right) \frac{d\Theta}{dt} = \alpha r |\Theta|^{n+1}. \quad (5.11)$$

Equation (5.11) describes the evolution of $\Theta(t)$ in the shutdown regime, $t > t_2$. In a similar manner to the analysis of § 4.2, we extrapolate solutions back to $t < t_2$, and apply an initial condition $\Theta(t_0) = -1$, where $t_0 < t_2$ is a virtual origin. The solution to (5.11) is then given implicitly by

$$\sum_{k=1}^n \left[\frac{C_+^k}{k\Theta^k} (1 - |\Theta|^k) \right] + \ln \left[\frac{C_+ + |\Theta|}{|\Theta|(1 + C_+)} \right] = -\frac{\alpha r (-C_+)^{n+1}}{1 + C_+} (t - t_0). \quad (5.12)$$

The height of the interface $h(t)$ is related to the interior concentration $\Theta(t)$ by (5.10). Using (5.6), the flux $F(t)$ is related to $\Theta(t)$ by

$$F = \alpha r Ra_0 |\Theta|^{n+1}. \quad (5.13)$$

Figure 10 shows solutions calculated from (5.12) for $\Theta(t)$, $F(t)$ and $h(t)$. The concentration $\Theta(t) < 0$ increases monotonically towards $\Theta(t \rightarrow \infty) = 0$, while the corresponding interfacial height $h(t)$ increases monotonically towards $h(t \rightarrow \infty) = h_\infty = 1 + 1/C_+$, independent of n . In the limit of large C_+ , which physically corresponds to the limit $(C_+^* - C_m^*) \gg (C_m^* - C_-^*)$, (5.12) reduces to the solution for a stationary interface (4.14), and the height h of the interface remains approximately constant for all time. For any value of C_+ , the evolution of the system is ultimately given by the solution for a fixed interface (4.14) (up to an additional factor of $1/h_\infty$ multiplying $t - t_0$), since $h \rightarrow h_\infty$ at long times.

The predictions for a stationary interface from § 4.2 are also shown for Θ and F in figure 10(a,b). Given the relatively large change in the interfacial height h over time (figure 10c), it is surprising that the interior concentration Θ (figure 10a) does not display a significant difference to the prediction for a stationary interface. This observation is related to the differences in the solute flux (figure 10b) between the

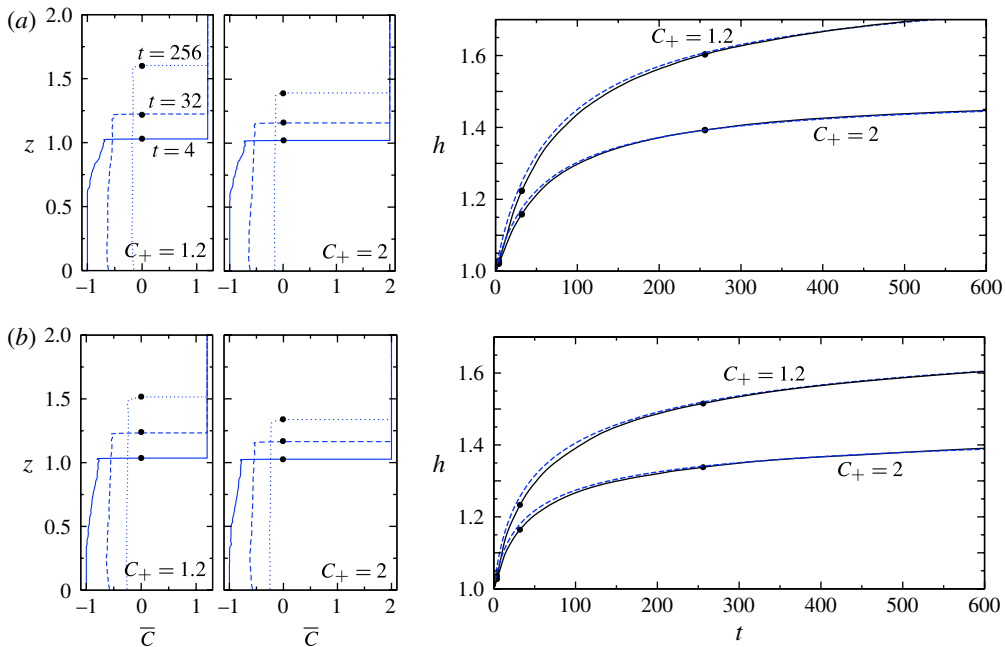


FIGURE 11. (Colour online) Numerical measurements for the immiscible system with a flat interface for $Ra_0 = 2 \times 10^4$, domain width $L = 2$ and height $H = 2$, showing the horizontally averaged concentration $\bar{C}(z, t)$ at times $t = 4$ (solid), $t = 32$ (dashed) and $t = 256$ (dotted), and the interfacial height $h(t)$: (a) linear equation of state $n = 1$; and (b) quadratic equation of state $n = 2$. Dashed lines show the theoretical predictions for the interfacial height $h(t)$ from box models. The dots on the left-hand figures show the location of the interface, and correspond to the dots on the right-hand figures. Each panel shows results for both $C_+ = 1.2$ and $C_+ = 2$, as marked.

predictions for a moving and a stationary interface: while the area of the domain below the interface ($\propto h$) is greater in the former case than in the latter, the flux F across the interface is also greater, and therefore the interior concentration Θ is not significantly different. For larger values of C_+ (not shown here), we find that the solutions of (5.11) increasingly resemble those for a stationary interface.

The dependences of Θ and F on n are also qualitatively similar to those for a stationary interface, which was discussed in §4.2.3. The interior concentration and the flux again have long-time behaviours $\Theta \sim t^{-1/n}$ and $F \sim t^{-(n+1)/n}$ to leading order, and the initial decay of the flux is again more rapid for larger n .

5.1.2. Numerical results

We solved the full governing equations for the flat-interface immiscible system numerically as outlined in appendix A. These equations are (3.11) and (3.14) for the convecting region $z < h(t)$, subject to boundary conditions $C = 0$ and $w = 0$ imposed at a flat interface $h(t)$, which is determined from (5.3).

Figure 11 shows measurements of the horizontally averaged concentration $\bar{C}(z, t)$ and the interfacial height $h(t)$ for both linear ($n = 1$) and quadratic ($n = 2$) equations of state. The upwards retreat of the interface is approximately linear at early times ($t < t_2$), while the downwelling plumes are descending through unmixed fluid. Once the system enters the shutdown regime ($t > t_2$), the behaviour of $h(t)$ changes. The

interface moves more slowly for larger values of C_+ , as there is more solute per unit volume in the upper layer. The corresponding profiles of $\bar{C}(z, t)$ show that the interior of the domain is well mixed for $t > t_2$, in agreement with the behaviour below a fixed interface (§ 4) and with the well-mixed assumption (5.4). The predictions of the theoretical box model for the interfacial height $h(t)$, which is based upon this well-mixed assumption, are also shown in figure 11, and give very good agreement with the numerical simulations.

5.2. Miscible system

When the two fluids are miscible, the relatively low concentration below the moving interface can affect the concentration field above the interface by diffusion. Since, by assumption, the interface $z = h(t)$ remains flat, the concentration C is independent of x for $z \geq h$. In this region, the governing transport equation (3.11) therefore reduces to a one-dimensional partial differential equation describing vertical diffusion away from the moving interface $h(t)$. In the frame of reference moving with the interface, (3.11) becomes

$$\frac{\partial C}{\partial t} - \frac{dh}{dt} \frac{\partial C}{\partial z} = \frac{1}{Ra_0} \frac{\partial^2 C}{\partial z^2}. \quad (5.14)$$

5.2.1. Theoretical box model

The development of a theoretical box model for the miscible system follows similar reasoning to that for the immiscible system in § 5.1.1. The horizontally averaged interior concentration $\Theta(t) \leq 0$ (5.4), the time-dependent Rayleigh number $Ra(t)$ (5.5) and the time-dependent Nusselt number $Nu(t)$ (5.6) are all as defined in § 5.1.1. The evolution equation for the average interior concentration $\Theta(t)$ is again given by (5.8).

Unlike the immiscible system, the concentration above the interface does not remain constant. Instead, it evolves by diffusion (5.14), and varies over some length scale between $C = 0$ at the interface and $C = C_+$ (as shown schematically in figure 1c). In order to generate a simple box model that approximates the solution of (5.14), we define a diffusive boundary-layer depth

$$\delta(t) = \frac{2}{C_+} \int_h^H (C_+ - C) dz, \quad (5.15)$$

which is an integral measure of the length scale of the concentration profile in $z > h$. We then approximate (5.14) by assuming that the evolution of δ can be described by a simple ordinary differential equation of the form

$$\frac{d\delta}{dt} = \frac{a_1}{Ra_0\delta} - a_2 \frac{dh}{dt}, \quad (5.16)$$

where a_1 and a_2 are numerical coefficients. Equation (5.16) is motivated by the physical balances that control the boundary-layer depth δ : the first term on the right-hand side of (5.16) describes the diffusive growth of a boundary layer with a flux proportional to the diffusivity Ra_0^{-1} and the concentration gradient, while the second term describes the advection of the interface.

The constants a_1 and a_2 in (5.16) are chosen so that the total solute $\delta C_+/2$ contained in the boundary layer gives a good approximation to that in the full solution of (5.14). We find a_1 and a_2 by comparing solutions of (5.16) with analytic solutions of (5.14) in two limits. In the limit where dh/dt is negligible, the pure-diffusion solution of (5.14) has the form $C \sim \text{erf}[(z - h)\sqrt{Ra_0/4t}]$, and (5.16)

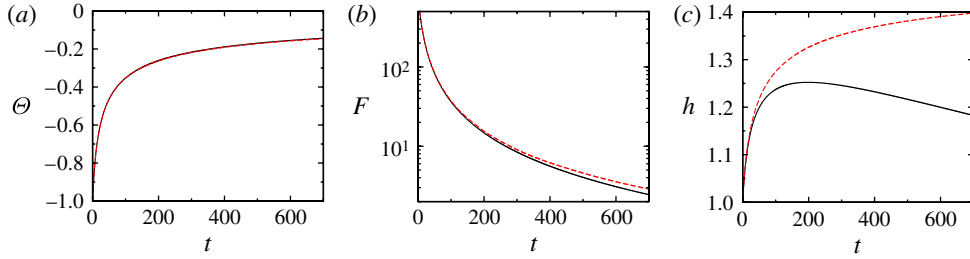


FIGURE 12. (Colour online) Theoretical predictions for the immiscible (dashed) and miscible (solid) systems, with $n = 2$, $C_+ = 2$, $t_0 = 0$ and $Ra_0 = 2 \times 10^4$: (a) the average concentration $\Theta(t)$, for which the two predictions are almost indistinguishable; (b) the solute flux $F(t)$; and (c) the interfacial height $h(t)$, which has qualitatively different late-time behaviour in the two systems.

gives $\delta = \sqrt{2a_1 t / Ra_0}$. Similarly, in the steady limit in which advection balances diffusion, the solution of (5.14) has the form $C \sim \exp[-\dot{h}Ra_0(z - h)]$, where $\dot{h} = dh/dt$, while (5.16) gives $\delta = a_1/a_2\dot{h}Ra_0$. We use (5.15) to equate each of these solutions at leading order, which gives $a_1 = 8/\pi$ and $a_2 = a_1/2 = 4/\pi$.

Including the contribution from the diffusive upper boundary layer, global conservation of solute (5.2) gives

$$h(C_+ + |\Theta|) = (1 + C_+) - \frac{\delta C_+}{2}. \tag{5.17}$$

After rearranging (5.8), (5.16) and (5.17), we extract coupled evolution equations for the concentration Θ , the height of the interface h and the diffusive boundary layer depth δ :

$$\frac{d\Theta}{dt} = \frac{|\Theta|\mathcal{N}}{h^2 Ra_0}, \tag{5.18}$$

$$\left(|\Theta| + C_+ - \frac{a_2 C_+}{2} \right) \frac{dh}{dt} = -\frac{a_1 C_+}{2\delta Ra_0} + \frac{|\Theta|\mathcal{N}}{h Ra_0}, \tag{5.19}$$

$$\left(|\Theta| + C_+ - \frac{a_2 C_+}{2} \right) \frac{d\delta}{dt} = \frac{a_1(C_+ + |\Theta|)}{\delta Ra_0} - \frac{a_2|\Theta|\mathcal{N}}{h Ra_0}. \tag{5.20}$$

Equations (5.18)–(5.20) give a theoretical prediction for the evolution of shutdown in a miscible flat-interface system. We integrate these equations numerically using the functional form $\mathcal{N}(Ra)$ in (4.12).

The solutions for the interior concentration Θ and the flux F from this model (figure 12a,b) are almost indistinguishable from those for the immiscible system. However, the interfacial height h for the miscible system exhibits qualitatively different behaviour at long times (figure 12c). The diffusion of solute above the interface slows the upward motion of the interface, and eventually leads to a decrease in the isopycnal that defines h . Equation (5.19), together with (5.6), give an equation for dh/dt , which shows that the height of the interface will decrease when

$$F < \frac{a_1 C_+}{2\delta}, \tag{5.21}$$

i.e. the height of the interface will decrease when the flux of solute into the lower layer (F) is less than the diffusive flux into the upper layer ($\sim C_+/\delta$).

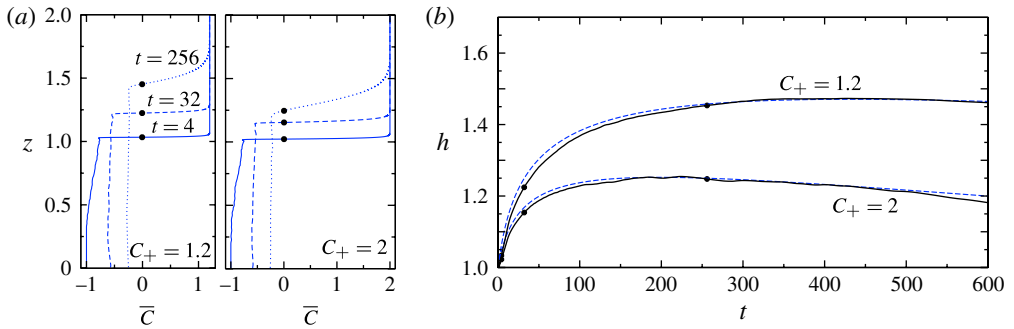


FIGURE 13. (Colour online) Numerical measurements for the miscible system with a flat interface, for $Ra_0 = 2 \times 10^4$, domain width $L = 2$ and height $H = 2$, and a quadratic equation of state $n = 2$: (a) the horizontally averaged concentration $\bar{C}(z, t)$ at times $t = 4$ (solid), $t = 32$ (dashed) and $t = 256$ (dotted); and (b) the interfacial height $h(t)$. Dashed lines show the theoretical predictions for the interfacial height from box models. The dots in panel (a) show the location of the interface, and correspond to the dots in panel (b). Each panel shows results for both $C_+ = 1.2$ and $C_+ = 2$, as marked.

In a finite system with no-flux boundaries, the final steady state must have a uniform concentration C_∞ , which is determined by conservation of solute (5.2) to be

$$C_\infty = \frac{-1 + (H - 1)C_+}{H}. \quad (5.22)$$

If $C_\infty < 0$, then the interface $z = h(t)$ must reach the upper boundary $z = H$, and (5.21) is never satisfied. Conversely, if $C_\infty > 0$, the interface must eventually descend, and approaches the base of the domain by diffusion. From (5.22), $C_\infty > 0$ if $H > 1 + 1/C_+$. This condition is satisfied for all the results presented in this paper.

5.2.2. Numerical results

We solved the full governing equations for the miscible system numerically (see appendix A). These equations are (3.11) and (3.14) for $z < h(t)$, and (5.14) for $z > h(t)$, together with conservation of solute (5.2), and the flat-interface assumption $w = 0$ at $z = h(t)$.

Figure 13 shows measurements of the horizontally averaged concentration $\bar{C}(z, t)$ and the interfacial height $h(t)$, with a quadratic equation of state $n = 2$. As in the case of the immiscible system (figure 11), the rate of upwards retreat of the interface is approximately constant for $t < t_2$, and then decreases once the system enters the shutdown regime ($t > t_2$). Unlike the immiscible system, however, the concentration field above the interface evolves in time (figure 13a). This evolution becomes very significant at long times, and results in an eventual decrease of the interfacial height $h(t)$ (figure 13b). The time at which the interface begins to descend decreases with increasing C_+ , as predicted by (5.21). The predictions of the box model are also shown in figure 13b, and accurately capture both the slowing of the interface and its eventual descent.

5.3. Conclusions for immiscible and miscible systems with a flat interface

The results in figures 11 and 13 show that the theoretical box models give excellent predictions for the shutdown of free-interface systems, under the assumption that the interface remains flat. These figures also highlight the main difference between the

immiscible and miscible systems: the long-time evolution of the interfacial height $h(t)$, which continually increases in the immiscible system, but eventually decreases in the miscible system. Given this qualitative difference in the interfacial behaviour, it is remarkable that the solute flux $F(t)$ and the interior concentration $\Theta(t)$ are so similar between the two systems (figure 12). The time scales for the shutdown of convection in the two systems are therefore roughly equal, even though observations of the interfacial height $h(t)$ might suggest otherwise. In the limit of large C_+ , we find that the predictions of the box models for these free-interface systems can be well approximated by the solution in § 4.2 for a fixed interface.

These results apply when the assumption of a flat interface is appropriate. In the next section, we examine miscible systems with a deformable interface, and show that the removal of the flat-interface approximation can lead to very different rates of shutdown.

6. Free-interface systems II: deformable interface

In this section we relax the flat-interface assumption. Therefore, the interface is free to ‘deform’, and solute can be entrained across it.

In § 6.1 we present numerical results for the miscible system. In § 6.2, to test the validity of the numerical results in a physical system, we compare with measurements from an experimental miscible system in a Hele-Shaw cell. In § 6.3, we consider the validity of the flat-interface approximation for miscible systems and discuss the anticipated effects of a deformable interface on immiscible systems.

6.1. Numerical results for the miscible system

We solved the governing equations (3.11) and (3.14) over the whole domain, with an initial condition given by (3.13) and a quadratic equation of state ($n = 2$) (see appendix A for numerical details). As discussed in § 2, the interfacial height $z = h(x, t)$ is defined by the contour of maximum density $\rho = \rho_m$, which is a function of horizontal position. We therefore define the average interfacial height $z = \bar{h}(t)$ to be the height at which the horizontally averaged density is maximum (which corresponds to the height at which $\bar{C}(z, t) = 0$).

Snapshots of the concentration field (figure 14a) show that there can be significant interfacial deformation in the miscible system. The extent of the deformation decreases with increasing C_+ . The dominant wavelength of the deformed interface appears to be set by the lateral spacing of the descending megaplumes. The average interfacial height $\bar{h}(t)$ and the interior concentration $\Theta(t)$ are compared with predictions from the miscible box model under a flat-interface approximation in figure 14(b,c). Both variables increase significantly more rapidly than the box model predicts, which suggests that the total solute flux $F(t)$ is initially much greater than with a flat interface. Measurements of $F(t)$ from the numerical simulations (not shown here) suggest that the initial flux is approximately three times as large than with a flat interface when $C_+ = 1.2$, and approximately twice as large when $C_+ = 2$.

6.2. Experimental results for the miscible system

In order to explore the effects of a deformable interface further, and to corroborate the numerical results of § 6.1, we conducted an experiment in a Hele-Shaw cell using two miscible fluids: propylene glycol (PPG) and water. Backhaus *et al.* (2011) used these fluids to examine the onset of convection and the evolution of the initial convective plumes. Neufeld *et al.* (2010) used a similar system, composed of water with a

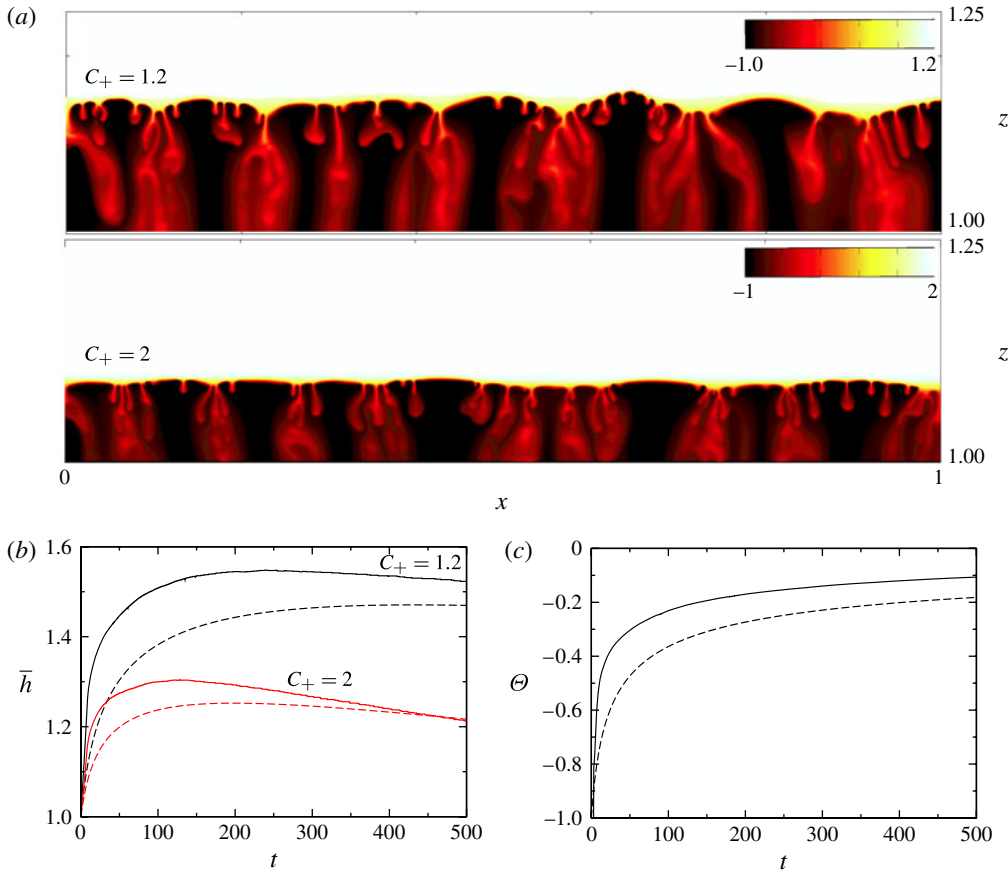


FIGURE 14. (Colour online) Numerical results at $Ra_0 = 2 \times 10^4$, domain width $L = 2$ and height $H = 2$, and a quadratic equation of state $n = 2$: (a) snapshots of the concentration profile at $t = 5$, for $C_+ = 1.2$ and $C_+ = 2$, showing significant deformation of the interface; (b) the average interfacial height $\bar{h}(t)$ (solid) for $C_+ = 1.2$ and $C_+ = 2$, together with the height predicted by the miscible theoretical box model (dashed); and (c) the interior concentration $\Theta(t)$ (solid) for $C_+ = 1.2$, together with the prediction of the miscible theoretical box model (dashed).

mixture of methanol and ethylene glycol, to examine the convective flow for $t_c < t < t_2$. Here, in contrast, we examine the long-time evolution of the system in the shutdown regime.

The experimental system consists of two glass sheets, separated by a shim of thickness $l = 0.41$ mm. The cell has width $L^* = 40$ cm and height 80 cm. The flow in the gap satisfies Darcy's law (3.1), with an effective permeability $\Pi = l^2/12 = 1.4 \times 10^{-4}$ cm² and porosity $\phi = 1$. PPG, of density $\rho_-^* = 1.0367$ g cm⁻³, filled the lower layer of the cell up to a depth $h_0^* = 32.5$ cm. The PPG was overlain by a layer of water, of density $\rho_+^* = 0.9995$ g cm⁻³, up to a total depth $H^* = 66$ cm. We define the concentration C^* to be the proportion of water by weight, so that the concentration of pure PPG is $C_-^* = 0$ and that of water is $C_+^* = 1$. Measurements of the density for different concentrations are shown in figure 15, together with a cubic fitting equation $\rho^* = f^*(C^*)$. The maximum density is obtained at $C_m^* \approx 0.25$,

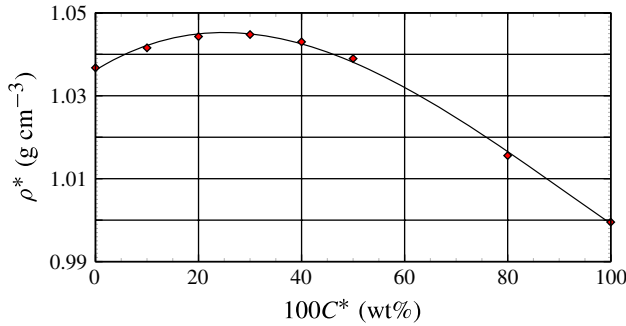


FIGURE 15. (Colour online) Relationship between density and concentration for the PPG–water system. Concentration $C^* = 1$ corresponds to pure water. Symbols denote measurements made in a densitometer, of which the curve is a cubic fit $\rho^* = f^*(C^*) = \rho_-^*(1 + 0.077C^* - 0.173C^{*2} + 0.062C^{*3})$, with $\rho_-^* = 1.036 \text{ g cm}^{-3}$.

and is given by $\rho_m^* = 1.0451 \text{ g cm}^{-3}$. The diffusivity of PPG in water varies a little with concentration, but is roughly constant between $C_-^* = 0$ and $C_m^* = 0.25$, with an approximate value $D = 2.5 \times 10^{-6} \text{ cm}^2 \text{ s}^{-1}$ (Wang *et al.* 2010).

We measured the average interfacial height $\bar{h}^*(t)$ and the interior concentration $\Theta^*(t)$ by the addition of blue dye to the water. The ambient temperature varied by less than $2 \text{ }^\circ\text{C}$ for the duration of the experiment (about three weeks). The experiment was set up by injecting both fluids into the cell from the top: the cell was first filled with the layer of PPG, which was allowed to settle; the overlying layer of water was then added over a period of some tens of seconds. Setting the experiment up in this way led to some initial local mixing and interfacial deformation, the effects of which decayed over $\sim 10 \text{ min}$; from then onwards the flow was dominated by downwelling fingers spread uniformly across the cell, and the interface was horizontal, except for the local deformation. This time over which the start-up transients decayed is much less than the time taken for the plumes to reach the base of the cell ($t_1^* \approx 8\text{--}9 \text{ h}$).

We also performed numerical simulations to compare with the experimental results (figure 16). In order to make a fair comparison, we estimate the effects of two physical processes in the experimental system. Firstly, the viscosity of aqueous PPG depends strongly on concentration. Pure PPG has viscosity $\mu \approx 0.05 \text{ Pa s}$, while the solution with the maximum density has viscosity $\mu \approx 0.015 \text{ Pa s}$ (Sun & Teja 2004). Therefore, the average viscosity below the interface will decrease over time as the average concentration increases. Secondly, experimental measurements of the velocity of the downwelling plumes suggest that Taylor dispersion (Taylor 1953) will act to increase the effective diffusivity by a factor of 2–3. An estimate of both of these effects, together with the parameters presented above, gives an initial Rayleigh number $Ra_0 \approx 2 \times 10^4$, and a convective time scale $T^* \approx 2.2 \text{ h}$. The numerical simulations used this initial value of Ra_0 , together with the equation of state $\rho = f(C)$ (figure 15) and an upper concentration $C_+ = 3$.

In order to give a simple approximation of the change of viscosity over time, we assume that the relevant viscosity scale is given by the average viscosity of all the fluid below the interface, and that the viscosity varies linearly with $1/\Theta^*(t)$. Since Ra_0 is inversely proportional to the viscosity, the value of the Rayleigh number Ra_0 in the simulations was changed over time, such that it increased linearly with the average concentration $\Theta(t)$. This simple approximation is not intended to reproduce the exact

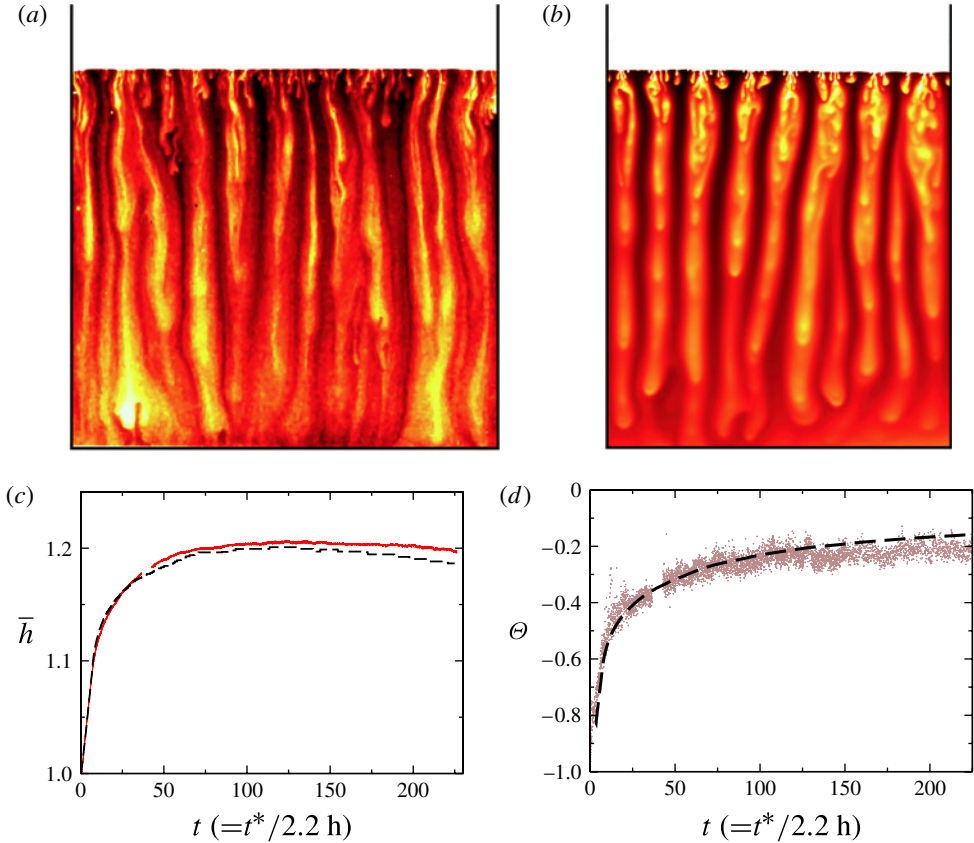


FIGURE 16. (Colour online) Comparison of experimental and numerical results: (a) an image-processed snapshot of the lower half of the experimental set-up, at time $t = 8$ ($t^* \approx 18$ h), which roughly marks the transition to the shutdown regime; (b) a snapshot from the numerical calculations described in the text, with domain width $L = 1$ and height $H = 2$, at time $t = 8$; (c) the dimensionless average height of the interface $\bar{h}(t)$, from the experiment (solid) and from the numerical calculations (dashed); (d) the interior concentration $\Theta(t)$, from the experiment (scattered points) and from numerical calculations (dashed line).

evolution of the experimental system, but rather to provide a reasonable qualitative estimate of the effects of viscosity variation.

The dynamical structure of the flow and the profile of convection in the experimental system are very similar to those in the numerical simulations (figure 16*a,b*). The average interfacial height $\bar{h}(t)$ and the interior concentration $\Theta(t)$ (figure 16*c,d*) similarly show excellent agreement between the experimental and numerical measurements. The transition to the shutdown regime can be observed at $t_2 \approx 8$ by the change in behaviour of the average interfacial height \bar{h} (figure 16*c*): before this time the upward retreat of the interface is approximately linear. At much later times, both the experimental and numerical measurements show that the interface slows down and eventually the height starts to decrease.

The initial linear upward retreat of the interface agrees qualitatively with the numerical observations in § 5.2.2, and the eventual decrease of the interface agrees

qualitatively with the predictions from the miscible box model in § 5.2.1. We note, however, that the time $t_2 \approx 8$ is much earlier than the predictions and numerical measurements of t_2 in § 5, because of the enhanced solute flux through the deformable interface here.

6.3. Discussion of systems with a deformable interface

The above results show that the effects of a deformable interface can be very significant for the miscible system. The excellent agreement between the numerical and experimental results with a deformable interface corroborates this observation.

We suggest that the removal of the flat-interface assumption leads to a significantly larger solute flux for two main reasons. Firstly, interfacial deformation results in the sloping of isopycnals below the interface, which leads to a baroclinic generation of lateral flow along the sloping boundary layer, and so an enhancement of the diffusive flux through the interface. (The simple increase in the length of the interface due to deformation is too small to account for the significant increase in flux.) Secondly, there is a contribution to the flux from material transport: positively buoyant fluid from above the interface can be entrained down across the interface. As the fluid loses solute by diffusion to its surroundings, its density increases because of the non-monotonic equation of state, and it continues to descend. It is difficult to quantify the relative importance of these two effects to the increase of the solute flux.

The interface deforms due to the competing effects of the stabilizing density gradients above the interface and the density gradients between upwelling and downwelling plumes that drive convection below the interface. If the stabilizing density gradient is much greater than the driving density gradients, then we expect both the interfacial deformation and any entrainment across the interface to be small. This prediction is given credence by the numerical results of § 6.1, which show that the interfacial deformation, and the corresponding enhancement of the solute flux, are less at larger values of C_+ . These observations suggest that the approximation of a flat interface is likely to be more appropriate for larger C_+ in the miscible system.

We have not examined the immiscible system with a deformable interface in this paper. In order to model this system numerically, we would need a different approach from that used in the rest of the paper, as the free interface would need to be tracked in both space and time, and the domain over which the equations were to be solved would no longer have a flat upper boundary.

We can, however, consider the expected effects of a deformable interface in an immiscible system. At the interface, there is a constant stable density jump $1 + |\rho_+|$, which is always greater than the typical density differences (<1) between upwellings and downwellings that drive convection. We therefore anticipate that the interface will remain approximately planar, and that the approximation of a flat interface will be appropriate for immiscible systems, particularly if $|\rho_+|$ is large. This observation highlights an important difference between the immiscible and miscible systems.

7. Discussion and conclusions

One-sided porous convection at high Rayleigh number bears many of the dynamical signatures of the statistically steady two-sided RB cell. We have used this observation to develop theoretical box models that describe the shutdown of complex one-sided convective systems, by coupling the evolution of the interior concentration with the flux through the boundary layer. These theoretical models, together with our numerical and experimental tools, have allowed for the examination of a variety of different

physically motivated systems, in which the active interface is either fixed or is free to move.

In the first part of this paper, we have shown that measurements of the Nusselt number $Nu(Ra)$ from the statistically steady two-sided RB cell can be used to accurately predict the shutdown of the flux $F(t)$ in one-sided convective systems. We find that these measurements, taken from Hewitt *et al.* (2012), are extremely well fitted by $Nu = \alpha Ra + \beta$, with $\alpha = 6.9 \times 10^{-3}$ and $\beta = 2.75$. Provided $Ra > 10^3$, this relationship can be approximated by setting $\beta = 0$. We have shown that this relationship $Nu(Ra)$ not only qualitatively describes the decay of the flux $F(t)$ in the one-sided shutdown system, but also can be used to give very good quantitative agreement with the results of numerical calculations.

Furthermore, we have found that the dynamical structure of the flow in the shutdown regime can be accurately described by the structures of an RB cell: the shutdown regime is dominated by downwelling megaplumes with an average horizontal wavenumber $k(t)$, which decreases over time in quantitative agreement with the measurements of the wavenumber $k(Ra)$ from an RB cell. This observation may help to shed light on the physical control of the dominant wavenumber in an RB cell, which remains unclear (Hewitt *et al.* 2012; Wen *et al.* 2012).

In both fixed-interface and free-interface systems, we have characterized the effect of different power-law equations of state, $\rho = 1 - (-C)^n$, on the flux of solute, and thus on the time scale for shutdown. We have found that, while the rate of shutdown is initially more rapid for larger values of n , at late times the flux decreases more slowly. For a fixed-interface system, which was considered in § 4, the initial linear rate of decrease of the flux scales like $(n + 1)^3$, while at long times the flux decreases like $t^{-(n+1)/n}$. This behaviour is qualitatively similar for free-interface systems. We find that the time scale for shutdown ($\sim \alpha^{-1}$) is, in all cases, much greater than the convective time scale (~ 1). This observation is a result of the relative ‘inefficiency’ of the flux, as described by the small coefficient α in the relationship (4.10) for the Nusselt number in an RB cell.

In the second part of the paper, we used the techniques developed in the earlier sections to consider two different free-interface systems, comprising immiscible or miscible fluids. In § 5, we examined both of these systems under the assumption that the interface, as defined in § 2, remained flat. Our models predict very similar behaviour for the flux over time between the immiscible and miscible systems. In the limit of large C_+ , the models can be very reasonably approximated by the solution for a fixed interface. Physically, this limit corresponds to the case when the concentration of maximum density C_m^* is much closer to the concentration of the lower layer C_-^* than to that of the upper C_+^* .

We have shown, however, that the evolution of the interfacial height $h(t)$ in the two systems is qualitatively different at long times: in the immiscible system, the height increases for all time, while in the miscible system, it eventually decreases, provided H is sufficiently large, even though the flux of solute across the interface into the lower layer remains positive. This observation provides an important difference when comparing the two systems, as discussed below.

In § 6, we relaxed the assumption of a flat interface. We presented numerical simulations of the miscible system, which show that the interfacial height eventually decreases, in qualitative agreement with the predictions of our theoretical box model. However, the solute flux is much larger than the box model predicts. This observation was corroborated by experimental results from a Hele-Shaw cell, which show excellent agreement with full numerical simulations. We suggest that the enhancement of the

flux in the miscible system is due to entrainment across the interface and sloping isopycnals below the interface, as discussed in § 6.3. These effects are the result of a balance between the stabilizing density gradients above the interface and the driving density gradients between the interleaving plumes below the interface.

In immiscible systems, however, these density gradients are not comparable, as there is a stabilizing discontinuity in the density ($1 + |\rho_+|$) across the interface, which will dominate, particularly if $|\rho_+|$ is large. Therefore, we anticipate that the interface will remain approximately planar and entrainment across it will be negligible, in agreement with the assumptions of a flat interface.

The relative applicability of the flat-interface approximation, and the long-time behaviour of the interfacial height $h(t)$, each provide an important difference between the immiscible and miscible systems, and suggest that care should be taken when modelling immiscible systems with a miscible analogue, or vice versa. For example, Neufeld *et al.* (2010) and Backhaus *et al.* (2011) each use miscible experimental systems to model the convective dissolution of CO_2 in a deep saline aquifer, which is an immiscible system. In the miscible experimental systems, we anticipate that the effects of interfacial deformation and entrainment would lead to a significant enhancement ($\approx 200\text{--}300\%$) of the solute flux. In contrast, in the CO_2 sequestration system, the stabilizing density difference between supercritical CO_2 and brine ($\sim 300 \text{ kg m}^{-3}$) is very much larger than the density contrasts that drive convection ($\sim 10\text{--}20 \text{ kg m}^{-3}$), and therefore we anticipate that interfacial deformation and entrainment would be negligible.

Under the assumption that capillary retention in the pore space can be ignored, and thus that the interface is ‘sharp’, the convective dissolution of CO_2 can be well described by our immiscible box model with a moving flat interface and a linear equation of state $n = 1$, presented in § 5.1. In addition, since CO_2 is only very weakly soluble in brine (3–5 % by weight), the value of C_+ for this system would be very large ($\sim 20\text{--}30$), and the flux would be well approximated by the solution for a fixed interface (4.15). In dimensional form, the total horizontally averaged solute flux for the fixed-interface system with $n = 1$ is given by

$$F^*(t) = \frac{4\alpha h_0^* T^* (C_m^* - C_-^*)}{(T^* + 4\alpha t)^2}, \quad (7.1)$$

where T^* is the convective time scale, given by $T^* = \phi h_0^* \Pi g \Delta \rho_m^* / \mu$ and $\alpha = 6.9 \times 10^{-3}$.

As an illustrative example, we use (7.1) to examine the time scales for shutdown in a high-permeability aquifer. We take representative parameter values from a high-permeability aquifer, such as the Utsira Sand reservoir at Sleipner, in the North Sea (Ennis-King & Paterson 2005; Bickle *et al.* 2007): $\Pi = 5 \times 10^{-12} \text{ m}^2$, $\phi = 0.3$, $g = 10 \text{ m s}^{-2}$, $\Delta \rho^* = 15 \text{ kg m}^{-3}$, $\mu = 5 \times 10^{-4} \text{ Pa s}$ and $D = 10^{-9} \text{ m}^2 \text{ s}^{-1}$. We consider a closed aquifer of depth $h_0^* = 100 \text{ m}$. The initial Rayleigh number is $Ra_0 \approx 6 \times 10^5$, and the convective time scale is $T^* \approx 0.6$ years. In such a closed aquifer, the transition to the shutdown regime would occur after roughly $t_2^* \approx 10$ years. After 20 years, the solute flux would have halved. After 75 years, it would be one-tenth of its initial value, and the interface would have retreated by nearly 3 m (3% of the original depth). These time scales correspond to the most permeable aquifers: some potential storage sites have permeabilities that are 2–3 orders of magnitude smaller than that considered here, in which case the transition to the shutdown regime would take thousands of years. These illustrative results apply to laterally confined aquifers, and,

while the physical processes that we have examined are still relevant, the time scales and dynamics of shutdown in laterally unconfined aquifers may differ substantially.

The models presented in this paper describe the shutdown of convection in a range of systems with different physical applications. Our theoretical, numerical and experimental results characterize the evolution of shutdown and the decay of the convective flux over time. The theoretical one-dimensional box models that we have derived provide analytically tractable tools that accurately capture the governing physics of the different complex convective systems. These simple models describe the relevant time scales of shutdown, and, for free-interface systems, the motion of the active interface. In the case of CO₂ sequestration, the models allow prediction of the rate of dissolution over time, and this dissolution has important implications for the stabilization of geologically stored CO₂.

Acknowledgements

The authors would like to thank M. Hallworth for invaluable help with the experimental work. D.R.H. is supported by a studentship from the EPSRC, and J.A.N. is supported by a University Research Fellowship from the Royal Society.

Appendix A. Numerical method

In this appendix we discuss the numerical scheme that we employed in the different sections of this paper. We begin by highlighting the differences in the numerical approach between each section, before describing the numerical method in more detail below.

In §§4 and 6, the governing equations (3.11) and (3.14) were solved throughout the domains $0 \leq z \leq 1$ and $0 \leq z \leq H$, respectively. In §5, however, (3.11) and (3.14) were solved below the interface $0 \leq z \leq h(t)$ only, in order to impose a flat interface at $z = h(t)$. Above the interface, the concentration either remains constant (immiscible system) or satisfies a one-dimensional advection–diffusion equation (5.14) (miscible system).

In order to accurately resolve the dynamics near to the interface $z = h$, we used a vertical coordinate transformation $\zeta(z, h)$. In §§4 and 5, the transformation from $\zeta \in [0, h]$ to $z \in [0, h]$ was similar to that used in Hewitt *et al.* (2012), and was given by

$$z = \frac{h}{2} \left[1 + \frac{\tanh[\eta(\zeta - h/2)]}{\tanh[\eta h/2]} \right], \quad (\text{A } 1)$$

where $\eta(Ra_0)$ is a stretching parameter that was chosen to ensure that sufficient points lay in the boundary layer below the interface. In §6, the governing equations were solved over the whole domain, and the interface was located in the interior. A more complex transformation is required to accurately resolve the boundary layers on either side of the interface, without dramatically increasing the computational cost. We employed a transformation of the form

$$z = \frac{H}{A_1 + A_2} \left\{ A_1 \frac{\tanh(a_1 \eta \zeta)}{\tanh(H a_1 \eta)} + A_2 \left[1 + \frac{\tanh(a_2 \eta [\zeta - H])}{\tanh(H a_2 \eta)} \right] \right\}, \quad (\text{A } 2)$$

where $\eta(Ra_0)$ is again a constant stretching parameter, and A_1 , A_2 , a_1 and a_2 are specified functions of the average interfacial height $\bar{h}(t)$, which were chosen to increase the resolution in a region centred on $z = \bar{h}$, and wider than the range of

any interfacial deformations. To reduce the computational cost, the transformation $\zeta[z, \bar{h}(t)]$ was not recalculated at every time step, but only when the interface $z = \bar{h}$ had moved a sufficient distance to require it. After each calculation of a new vertical discretization $\zeta(z, \bar{h})$, the variables were mapped from the previous discretization to the new grid using quadratic interpolation.

The governing equations (3.11) and (3.14) were transformed analytically to (x, ζ) coordinates and then solved on a uniform rectangular grid using horizontal and (transformed) vertical resolution Δx and $\Delta \zeta$, respectively. The Poisson equation (3.14) was solved for the streamfunction ψ using a fast Fourier transform for the x derivatives and a standard fourth-order finite-difference operator for the ζ derivative. Equation (3.11) was discretized using an alternating-direction implicit (ADI) method (Press *et al.* 1989), centred on the half time step to give second-order accuracy in time. The diffusion terms were spatially discretized using standard second-order finite-difference operators. The advection operator was discretized using a flux-conservative representation, which requires that the concentration and streamfunction be calculated at the centre and the vertices of grid cells, respectively. We used a second-order midpoint method to calculate the streamfunction at the half time step, which is a requirement of the ADI scheme. The boundary conditions for the concentration field were controlled by including an additional point in the centre of each grid cell around the outside of the domain: no-flux boundary conditions were thus imposed directly, while constant-concentration boundary conditions were imposed using a second-order extrapolation of the neighbouring points.

In § 5 (free-interface systems with a flat interface), the location of the interface $h(t)$ was found by global conservation of solute (5.2) at each time step. For the miscible system with a flat interface (§ 5.2), the one-dimensional transport equation (5.14) was solved at each time step using standard second-order finite-difference operators on a uniform grid above the interface.

The smallest horizontal scales are found in thin boundary-layer instabilities (protoplumes). In the shutdown regime, these horizontal length scales increase during the simulation as the density difference with the interior, and thus the effective Rayleigh number, decreases. The horizontal resolution was therefore chosen to ensure that these structures were well resolved at early times. Typical values of the horizontal and (transformed) vertical discretization at $Ra_0 = 2 \times 10^4$ are $\Delta x = (2048)^{-1}$ and $\Delta \zeta = (250)^{-1}$. The time step Δt was chosen to be smaller than the Courant time scale $\Delta x / \max|\mathbf{u}|$: at $Ra_0 = 2 \times 10^4$, the time step was $\Delta t = (1400)^{-1}$.

Appendix B. Discussion of the average interior concentration in a Rayleigh–Bénard cell

We consider a two-dimensional RB cell in a porous medium, containing a fluid that satisfies a dimensionless power-law equation of state $\rho = 1 - (-C)^n$, as in (3.10). The cell has periodic (or no-flux) boundary conditions on the sidewalls, and fixed concentrations on the upper and lower boundaries,

$$C(x, z = 1) = 0, \tag{B 1}$$

$$C(x, z = 0) = -1. \tag{B 2}$$

We consider the system in statistically steady state.

Hewitt *et al.* (2012) presented numerical results for the case of a linear equation of state ($n = 1$). They showed that, close to the upper and lower boundaries of the

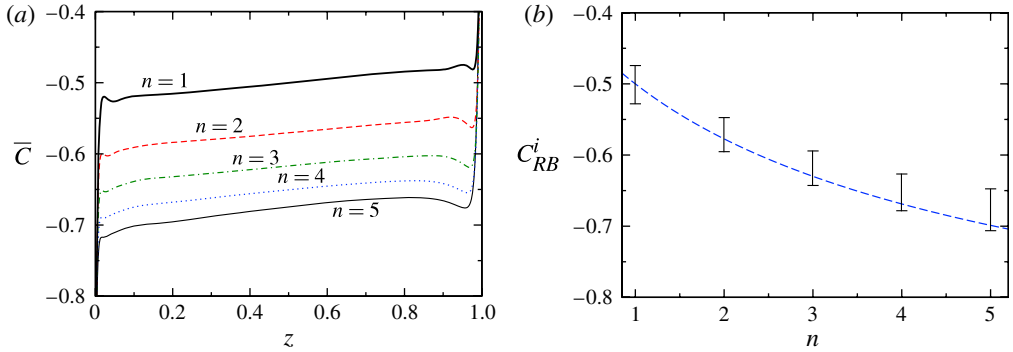


FIGURE 17. (Colour online) Numerical measurements from an RB cell, with $Ra = 10^4$: (a) the average concentration $\bar{C}(z)$ for different values of n as marked; (b) estimated range of the interior concentration $C_{RB}^i(n)$ in the linear interior region, taken from the measurements in panel (a), together with an approximate analytic fit $C_{RB}^i = -(n+1)^{-1/n}$ (dashed).

domain, the horizontally averaged concentration profile $\bar{C}(z)$ varies rapidly. However, in the interior of the domain, $\bar{C}(z)$ has a small linear gradient that decreases as the Rayleigh number Ra increases. In the limit $Ra \rightarrow \infty$, the average concentration in the interior tends to a constant value, $C_{RB}^i = -1/2$.

We have carried out numerical calculations of (3.11) and (3.14) in an RB cell for $1 \leq n \leq 5$, at Rayleigh number $Ra = 10^4$. Measurements of the interior concentration $\bar{C}(z)$ from these calculations are shown in figure 17(a). Based on the results for $n = 1$ discussed above, we make the assumption for $n > 1$ that the gradient of $\bar{C}(z)$ in the interior of the domain also decreases as Ra increases, and that, as $Ra \rightarrow \infty$, the average concentration in the interior tends to a constant value $C_{RB}^i(n)$. By extrapolating the linear interior gradient of $\bar{C}(z)$ for each value of n from our measurements in figure 17(a), we generate estimates for the range of possible values of $C_{RB}^i(n)$, as shown in figure 17(b). We find that an approximate analytic fit lying within this range is given by $C_{RB}^i = -(n+1)^{-1/n}$, which is also shown in figure 17(b). This curve provides a reasonable approximation for $n < 5$, which includes the physically important cases, $n = 1$ and $n = 2$. We use this approximate form for C_{RB}^i throughout the paper.

REFERENCES

- BACKHAUS, S., TURITSYN, K. & ECKE, R. E. 2011 Convective instability and mass transport of diffusion layers in a Hele-Shaw geometry. *Phys. Rev. Lett.* **106**, 104501.
- BICKLE, M., CHADWICK, A., HUPPERT, H. E., HALLWORTH, M. A. & LYLE, S. 2007 Modelling carbon dioxide accumulation at Sleipner: implications for underground carbon storage. *Earth Planet. Sci. Lett.* **255**, 164–176.
- CHENG, P. 1978 Heat transfer in geothermal systems. *Adv. Heat Transfer* **14**, 1–105.
- DUFFY, C. J. & AL-HASSAN, S. 1988 Groundwater circulation in a closed desert basin: topographic scaling and climatic forcing. *Water Resour. Res.* **24**, 1675–1688.
- ENNIS-KING, J. P. & PATERSON, L. 2005 Role of convective mixing in the long-term storage of carbon dioxide in deep saline formations. *SPE J.* **10** (3), 349–356.
- FERNANDEZ, J., KUROWSKI, P., PETITJEANS, P. & MEIBURG, E. 2002 Density-driven unstable flows of miscible fluids in a Hele-Shaw cell. *J. Fluid Mech.* **451**, 239–260.

- GILFILLAN, S. M. V., SHERWOOD LOLLAR, B., HOLLAND, G., BLAGBURN, D., STEVENS, S., SCHOELL, M., CASSIDY, M., DING, Z., ZHOU, Z., LACRAMPE-COULOUME, G. & BALLENTINE, C. J. 2009 Solubility trapping in formation water as dominant CO_2 sinks in natural gas fields. *Nature* **458**, 614–618.
- GOLDSTEIN, B., HIRIART, G., BERTANI, R., BROMLEY, C., GUTIÉRREZ-NEGRÍN, L., HUENGES, E., MURAOKA, H., RAGNARSSON, A., TESTER, J. & ZUI, V. 2011 Geothermal energy. In *Renewable Energy Sources and Climate Change Mitigation: Special Report of the IPCC*, pp. 401–436. Cambridge University Press.
- GRAHAM, M. D. & STEEN, P. H. 1994 Plume formation and resonant bifurcations in porous-media convection. *J. Fluid Mech.* **272**, 67–89.
- HASSANZADEH, H., POOLADI-DARVISH, M. & KEITH, D. W. 2006 Stability of a fluid in a horizontal saturated porous layer: effect of nonlinear concentration profile, initial and boundary conditions. *Transp. Porous Med.* **65**, 193–211.
- HASSANZADEH, H., POOLADI-DARVISH, M. & KEITH, D. W. 2007 Scaling behaviour of convective mixing, with application to geological storage of CO_2 . *AIChE J.* **53**, 1121–1131.
- HEWITT, D. R., NEUFELD, J. A. & LISTER, J. R. 2012 Ultimate regime of high Rayleigh number convection in a porous medium. *Phys. Rev. Lett.* **108**, 224503.
- HILL, J. M. 1987 *One-Dimensional Stefan Problems: An Introduction*. Longman.
- HOWARD, L. N. 1964 Convection at high Rayleigh number. In *Applied Mechanics, Proceedings of 11th International Congress of Applied Mathematics* (ed. H. Görtler & P. Sorger). pp. 1109–1115. Springer.
- HUPPERT, H. E. 1989 Phase changes following the initiation of a hot turbulent flow over a cold solid surface. *J. Fluid Mech.* **198**, 293–319.
- HUPPERT, H. E. & SPARKS, R. S. J. 1988a The generation of granitic magmas by intrusion of basalt into continental crust. *J. Petrol.* **29** (3), 599–624.
- HUPPERT, H. E. & SPARKS, R. S. J. 1988b Melting the roof of a chamber containing a hot, turbulently convecting fluid. *J. Fluid Mech.* **188**, 107–131.
- KIMURA, S., SCHUBERT, G. & STRAUSS, J. M. 1986 Route to chaos in porous-medium thermal convection. *J. Fluid Mech.* **166**, 305–324.
- VAN DER MEER, B. 2005 Carbon dioxide storage in natural gas reservoirs. *Oil Gas Sci. Technol.* **60**, 527–536.
- METZ, B., DAVIDSON, O., DE CONINCK, H. C., LOOS, M. & MEYER, L. 2005 *Carbon Dioxide Capture and Storage: Special Report of the IPCC*. Cambridge University Press.
- NEUFELD, J. A., HESSE, M. A., RIAZ, A., HALLWORTH, M. A., TCHELEPI, H. A. & HUPPERT, H. E. 2010 Convective dissolution of carbon dioxide in saline aquifers. *Geophys. Res. Lett.* **37**, 22404.
- NEUFELD, J. A., VELLA, D., HUPPERT, H. E. & LISTER, J. R. 2011 Leakage from gravity currents in a porous medium. Part I. A localized sink. *J. Fluid Mech.* **666**, 391–413.
- NIELD, D. A. & BEJAN, A. 2006 *Convection in Porous Media*, 3rd edn. Springer.
- ORR, F. M. Jr. 2009 Onshore geologic storage of CO_2 . *Science* **325**, 1656–1658.
- OTERO, J., DONTCHEVA, L. A., JOHNSTON, H., WORTHING, R. A., KURGANOV, A., PETROVA, G. & DOERING, C. R. 2004 High-Rayleigh-number convection in a fluid-saturated porous layer. *J. Fluid Mech.* **500**, 263–281.
- PAU, G. S. H., BELL, J. B., PRUESS, K., ALMGREN, A. S., LIJEWSKI, M. J. & ZHANG, K. 2010 High-resolution simulation and characterization of density-driven flow in CO_2 storage in saline aquifers. *Adv. Water Resour.* **33**, 443–455.
- PRESS, W. H., FLANNERY, B. P., TEUKOLSKY, S. A. & VETTERLING, W. T. 1989 *Numerical Recipes (Fortran)*, 1st edn. Cambridge University Press.
- PRITCHARD, D. 2007 Gravity currents over fractured substrates in a porous medium. *J. Fluid Mech.* **584**, 415–431.
- RIAZ, A., HESSE, M. A., TCHELEPI, H. A. & ORR, F. M. Jr. 2006 Onset of convection in a gravitationally unstable diffusive layer in porous media. *J. Fluid Mech.* **548**, 87–111.
- SLIM, A. C., BANDI, M. M., MILLER, J. C. & MAHADEVAN, L. 2013 Dissolution-driven convection in a Hele-Shaw cell. *Phys. Fluids* (in press).

- SLIM, A. C. & RAMAKRISHNAN, T. S. 2010 Onset and cessation of time-dependent, dissolution-driven convection in porous media. *Phys. Fluids* **22**, 124103.
- SUN, T. & TEJA, A. S. 2004 Density, viscosity and thermal conductivity of aqueous solutions of propylene glycol, dipropylene glycol, and tripropylene glycol between 290 K and 460 K. *J. Chem. Engng Data* **49**, 1311–1317.
- TAYLOR, G. I. 1953 Dispersion of soluble matter in solvent flowing slowly through a tube. *Proc. R. Soc. Lond. A* **219**, 186–203.
- VELLA, D., NEUFELD, J. A., HUPPERT, H. E. & LISTER, J. R. 2011 Leakage from gravity currents in a porous medium. Part II. A line sink. *J. Fluid Mech.* **666**, 414–427.
- WANG, M.-H., SORIANO, A. N., CAPARANGA, A. R. & LI, M.-H. 2010 Binary mutual diffusion coefficient of aqueous solutions of propylene glycol and dipropylene glycol. *J. Taiwan Inst. Chem. Eng.* **41**, 279–285.
- WEN, B., DIANATI, N., LUNASIN, E., CHINI, G. P. & DOERING, C. R. 2012 New upper bounds and reduced dynamical modelling for Rayleigh–Bénard convection in a fluid-saturated porous layer. *Commun. Nonlinear Sci. Numer. Simul.* **17**, 2191–2199.
- WOODING, R. A., TYLER, S. W. & WHITE, I. 1997*a* Convection in groundwater below an evaporating salt lake: 1. Onset of instability. *Water Resour. Res.* **33**, 1199–1217.
- WOODING, R. A., TYLER, S. W., WHITE, I. & ANDERSON, P. A. 1997*b* Convection in groundwater below an evaporating salt lake: 2. Evolution of fingers or plumes. *Water Resour. Res.* **33**, 1219–1228.
- XU, X., CHEN, S. & ZHANG, Z. 2006 Convective stability analysis of the long-term storage of carbon dioxide in deep saline aquifers. *Adv. Water Resour.* **29**, 397–497.